Mitochondrial fusion in reactive astrocytes coordinates local metabolic domains to promote vascular repair

Jana Göbel[1], Patric Pelzer[1], Esther Engelhardt[1], Vignesh Sakthivelu[1], Hannah M. Jahn[1], Milica Jevtic[1], Kat Folz-Donahue[2], Christian Kukat[2], Astrid Schauss[1], Christian K. Frese[1], Alexander Ghanem[3], Karl-Klaus Conzelmann[3], Elisa Motori[2] and Matteo Bergami[1,4,5,*]

[1]Cologne Excellence Cluster on Cellular Stress Responses in Aging-Associated Diseases (CECAD), University Hospital Cologne, Joseph-Stelzmann-Str. 26, D-50931 Cologne, Germany.

[2]Max Planck Institute for Biology of Ageing, Joseph-Stelzmann-Str. 9b, D-50931 Cologne, Germany.

[3]Max von Pettenkofer Institute and Gene Center, Ludwig Maximilians-University Munich, Feodor-Lynen-Str. 25, D-81377 Munich, Germany.

[4]Institute of Genetics, Zülpicher Str. 47a, D-50674, University of Cologne, Germany

[5]Center for Molecular Medicine, Robert-Koch-Str. 21, 50931 Cologne, Germany

*Correspondence to: Matteo Bergami

CECAD-University Hospital of Cologne, Germany

Email: matteo.bergami@uk-koeln.de

Phone: +49 (0)221 478 84250

Abstract

Astrocytes have emerged for playing key roles in tissue remodeling during brain repair, however the underlying mechanisms remain poorly understood. We show that acute injury and blood-brain barrier disruption trigger the formation of a prominent mitochondrial-enriched compartment in astrocytic end-feet which enables vascular recovery. Integrated imaging approaches revealed that this mitochondrial clustering is part of a metabolic adaptive response regulated by fusion dynamics. Astrocyte-specific deletion of Mitofusin 2 (*Mfn2*) suppressed perivascular mitochondrial remodeling and altered mitochondria-endoplasmic reticulum tethering domains. Functionally, two-photon imaging experiments showed that these structural changes were mirrored by impaired mitochondrial Ca^{2+} uptake leading to abnormal cytosolic transients in astrocytic end-feet *in vivo*. At the tissue level, a severely compromised microvasculature in the lesioned area was rescued by boosting mitochondrial perivascular clustering in MFN2-deficient astrocytes. These data unmask a crucial role for astrocyte mitochondrial dynamics in regulating local metabolic signaling and have important implications for repairing the injured brain.

Introduction

By virtue of specialized contacts with neurons and the brain vasculature, astrocytes regulate essential aspects of brain energy metabolism (Belanger et al., 2011). Besides endothelial cells and pericytes, which constitute the actual blood-brain-barrier (BBB), astrocytic end-feet functionally ensheathe most of the cerebrovascular network and serve as specialized dynamic exchange sites for ions, water and energy substrates with brain parenchyma (Iadecola, 2017). Under physiological conditions these functions contribute to neurovascular coupling, whereby the Ca^{2+}-mediated astrocytic release of vasoactive molecules regulates – in synergy with other cell types – functional hyperaemia according to local neuronal activity and metabolic demand (Gordon et al., 2008; Mishra et al., 2016; Petzold et al., 2008; Takano et al., 2006). While maintenance of this tight coupling ensures the supply of metabolites across the gliovascular interface, the structural and functional changes experienced by perivascular end-feet following BBB disruption, as for instance during brain trauma or ischemia, are much less understood.

Following traumatic injury, the coordinated activity of all cell types that regulate vascular permeability becomes severely compromised, eventually resulting in BBB breakdown, intracerebral hemorrhage, secondary inflammation and neurodegeneration (Zhao et al., 2015). Under these settings, astrocytes are known to acquire so-called “reactivity states” which underlie important functions in the progression and possible resolution of the injury (Khakh and Sofroniew, 2015; Liddelow and Barres, 2017). During this response astrocytes undergo not only major changes in morphology and gene expression but also exhibit a significant extent of metabolic plasticity (Anderson et al., 2016; Bardehle et al., 2013; Hamby et al., 2012; Polyzos et al., 2019; Zamanian et al., 2012). In fact, while astrocytes utilize oxidative phosphorylation (OXPHOS) for their energy metabolism (Ignatenko et al., 2018; Lovatt et al., 2007), they can sustain for long periods of time glycolytic fluxes (Supplie et al., 2017), underscoring the capability of these cells to accommodate a significant metabolic rewiring depending on substrate availability and local energy needs (Hertz et al., 2007). This quite remarkable form of plasticity is emphasized by the fact that astrocytes responding to injury *in vivo* can adjust their metabolic signature by efficiently and reversibly modifying the architecture of their mitochondrial network (Motori et al., 2013; Owens et al., 2015),

i.e. the central hub for cellular energy metabolism and metabolic signaling, thus adding a new layer of complexity to our understanding of astrocytic reactivity to tissue challenges.

The architecture of the mitochondrial network in cells is usually very dynamic and its maintenance depends upon regulated fusion-fission events as well as on contact sites with the ER and other organelles (Labbe et al., 2014). In mammalian cells, the main drivers of mitochondrial membrane dynamics are mitofusins (MFN1 and MFN2) (Chen et al., 2003) and optic atrophy-1 (OPA1) (Cipolat et al., 2004) for mitochondrial fusion, while dynamin-related protein-1 (DRP1) is the key player in outer mitochondrial fission (Ishihara et al., 2009). Together, the coordinated action of these molecules shapes mitochondria towards more fragmented or elongated morphologies to match precise cellular metabolic needs (Dietrich et al., 2013; Gomes et al., 2011; Rambold et al., 2011). Functionally, this mitochondrial remodeling is also regulated by a physical tethering with ER membranes (Guo et al., 2018; Murley and Nunnari, 2016), which form specialized contact sites (so-called mitochondria-associated membranes or MAMs) that control important metabolic signaling functions including lipid trafficking as well as Ca^{2+} and ROS microdomains (Csordas et al., 2018). Intriguingly, evidence exists for complex mitochondrial and ER morphologies in astrocytes *in situ*, where these organelles have been found to reach fine perisynaptic processes and end-feet (Gobel et al., 2018; Lovatt et al., 2007; Mathiisen et al., 2010; Motori et al., 2013). Moreover, a role for astrocytic mitochondria in regulating the frequency of Ca^{2+} microdomains *in vivo* has been recently proposed (Agarwal et al., 2017). Yet, whether and to which extent a dynamic remodeling of these two organelles may effectively couple the acquisition of a reactive state in astrocytes with functional metabolic changes is unclear.

Here, we provide evidence that acute brain injury triggers a distinctive rearrangement of mitochondria in perivascular astrocytic end-feet, where they form extensive reciprocal contact sites with the ER. Our data indicate that this remodeling is coordinated by mitochondrial fusion dynamics and generates a local mitochondrial-enriched domain surrounding microvessels. *Mfn2* deficiency in reactive astrocytes alters the extent of mitochondria-ER tethering, prevents injury-induced perivascular accumulation of mitochondria and leads to disrupted Ca^{2+} dynamics in astrocyte end-feet, ultimately impairing vascular recovery in the injured area. Importantly, our data indicate that

vascular repair can be restored in absence of mitochondrial fusion by enhancing perivascular accumulation of astrocytic mitochondria. These results establish a mechanism for astrocytic mitochondrial fusion in orchestrating the metabolic adaptations of brain tissue *in vivo* and unravel a key role for astrocytes in sustaining microvasculature remodeling during repair.

Results

Astrocyte end-feet are naturally enriched in mitochondria-ER contact sites

In order to investigate in detail how the architecture of mitochondrial and ER networks may match the morphological complexity of astrocytes we utilized a virus-based strategy to label specifically these organelles *in vivo* (Figure 1A). Minimal amounts of either hGFAP promotor-driven adeno-associated viruses (AAV) or modified EnvA-pseudotyped rabies viruses (RABV) were stereotactically injected into the cortex of wild-type or hGFAP-TVA mice, respectively, to drive the expression of mitochondrial- or ER-targeted fluorophores (i.e. mitoRFP and ER-GFP). Both viral-based approaches have been previously shown to efficiently restrict the expression of transgenes to astrocytes in the adult brain (Motori et al., 2013; Shigetomi et al., 2013). Single-astrocyte analysis one week after virus delivery revealed a complex morphology of these organelles, which were found decorating the most peripheral astrocytic processes, including fine branchlets (Figure 1B). Interestingly, besides few primary branches originating from the soma, putative structures identified as perivascular end-feet (i.e., possessing a tube-like morphology) were particularly enriched in ER and mitochondria (Figure 1C). In these regions, the ER appeared to virtually delineate the shape of vessels, while mitochondria often formed a dense meshwork that was much similar to the one observed within primary branches rather than distally-located fine perisynaptic processes (branchlets) (Figure 1C). Experiments conducted by labelling the microvasculature via systemic dextran injection prior to sacrifice revealed that astrocytic ER and mitochondrial networks outlined the labelled vessels to the extent that often whole sections of the microvasculature appeared wrapped by a thin but discernible layer of astrocytic organelles (Figure 1D-E). In contrast, virus-mediated labelling of other organelles including peroxisomes and lysosomes yielded

a much different distribution, being largely confined to the cell body and major branches (Supp Figure 1A-D).

At the ultrastructural level, astrocytic end-feet appeared enriched with ER membranes surrounding not only the basal lamina but also most of mitochondria located within the perivascular process (Figure 1F and Supp Figure 1E-F). In particular, substantial portions of the mitochondrial perimeter were bordered by ER membranes and, at these contact sites, the two organelles maintained an average reciprocal distance of 18.9 ± 5.0 nm (Figure 1F). By comparison, both the size of mitochondria and the extent of ER membranes were smaller in perisynaptic astrocytic processes, resulting in visibly fewer contact sites, despite a similar mitochondria-ER average distance of 20.4 ± 7.0 nm at these sites (Figure 1G). Systematic quantification of these morphological parameters revealed a net enrichment in mitochondrial area and MAM domains within the end-feet (Figure 1H).

Marked remodeling of astrocyte mitochondrial networks following cortical injury

Astrocyte reactivity states are characterized by prominent changes in energy metabolism and mitochondrial network morphology (Castejon, 2015; Hamby et al., 2012; Motori et al., 2013; Zamanian et al., 2012). To explore the functional consequences of brain insults for perivascular organelle distribution, we utilized a genetic approach to conditionally express mitoYFP in adult astrocytes and follow the morphological changes of their mitochondria following stab-wound (SW)-injury (Figure 2A). To this aim, hGFAP-CreER mice (Chow et al., 2008) were crossed with mitoYFP floxed-stop mice (Sterky et al., 2011) and the resulting line was induced with tamoxifen at the age of 6-to-8 weeks. With this approach, about 88% of cortical astrocytes (S100β+) underwent recombination (Supp Figure 2A-B), allowing for a systematic analysis of the changes in their mitochondrial network both within the lesion core (i.e. the area mostly enriched in pro-inflammatory CD45+ leukocytes) and penumbra region surrounding the lesion track (in which GFAP was strongly upregulated) (Figure 2B). By one week following SW, when a clear distinction between these two regions was most pronounced (as compared to later time points), astrocytes displayed distinct behaviours with regard to their mitochondrial network: while astrocytes within the core

underwent overt mitochondrial fragmentation, astrocytes strongly immunoreactive for GFAP+ within the penumbra region maintained more elongated mitochondrial morphologies (Figure 2C). Yet, detailed morphometric analysis of reconstructed mitoYFP+ astrocytes revealed that, irrespective of their “metabolic” state (i.e., whether resting or reactive), the mitochondrial network in these cells was usually composed by highly heterogeneous morphologies, with both tubular and very long (up 8-10 μm) as well as much shorter organelles (less than 0.5 μm) (Figure 2C). This morphological diversity became apparent when plotting the length versus sphericity of the whole mitochondrial population of several reconstructed astrocytes selected for their proximity to the lesion track (Figure 2D): by 7 days post-SW the mitochondrial network displayed a significant shift towards fragmentation with over 60% of the whole mitochondrial population being <1 μm in length, in contrast to a 43.5% in control astrocytes (Figure 2D). In particular, this difference was most pronounced for peripheral processes (Figure 2C), where single mitochondria could be more easily discerned from the bulk of more interconnected organelles present in the soma and main branches. Whole-cell time-course analysis during a period ranging from 3 days to 2 months after SW-injury revealed that while the fraction of fragmented mitochondria sharply increased during the first week, the network was restored to levels comparable to control astrocytes by the third week (Figure 2E). This trend was mirrored by opposite changes in the proportion of tubular mitochondria, confirming that the evolving reactive state of astrocytes is accompanied by a time-dependent remodeling of the whole mitochondrial network over the course of several weeks after injury (Motori et al., 2013).

Interestingly, inspection of vessels proximal to the lesion revealed a marked accumulation of astrocytic mitochondria in perivascular end-feet (Figure 2F). In particular, analysis of vessel cross-sections disclosed that the extent of mitochondria surrounding the vascular lumen significantly increased by 7 and 28 days after SW (Figure 2G-H), the latter being a time when mitochondrial network morphology had already normalized back to control levels (Figure 2E). We next assessed whether the ER may also undergo a similar extent of remodeling in response to injury. Three-dimensional reconstruction of individual ER-GFP-expressing astrocytes in conjunction to dextran-labelling revealed the whole distribution of the ER network across distinct astrocytic

territories in uninjured hemispheres (Figure 2J and Supp Figure 2C). In these control samples, the GFP signal allowed for the assessment of a perivascular ER-GFP "*g*-ratio" to investigate changes in ER dynamics within the end-feet (Figure 2K). This analysis disclosed a time-dependent increase in the thickness of perivascular ER-GFP, which peaked by 7 days post-SW but reverted to near-basal conditions by 28 days (Figure 2K). These results were corroborated by analysing the relative volume distribution of the ER-GFP signal (i.e. signal density) across astrocytic compartments (Supp Figure 2D). In control astrocytes, perivascular end-feet accounted for 19.2% of all ER-GFP signal in individual cells (Supp Figure 2F). In contrast, in injury-induced reactive astrocytes an accumulation of ER-GFP signal was observed in the end-feet (35.9%) at the expenses of main branches (where the relative ER-GFP proportion decreased from 39.1% in controls to 25.2% in injured samples) (Supp Figure 2E-F). Interestingly, by 28 days after SW the relative distribution of ER-GFP signal mostly normalized (Supp Figure 2E-F), suggesting that in contrast to the enduring response of the mitochondrial network in perivascular end-feet (Figure 2H), remodeling of the ER compartment may only be temporary.

Astrocyte-specific deletion of *Mfn2* abrogates perivascular remodeling of mitochondria

The reversible transition of the mitochondrial network from fragmentation at 7 days post-SW to a tubular network by 21 days (Figure 2E), together with the peculiar remodeling of mitochondria within the end-feet of injured astrocytes (Figure 2G-H), argues in favour of regulatory mechanisms playing a role in adjusting their mitochondrial network to match evolving metabolic needs following injury. We reasoned that interfering with these mechanisms by preventing mitochondrial re-tubulation may provide a valid approach to dissect the specific role of this network remodeling for the astrocyte's physiology (Figure 3A). We opted for the conditional deletion of the GTPase protein MFN2, which is a key effector of mitochondrial outer membrane fusion dynamics but also regulates mitochondria-ER tethering domains (Schrepfer and Scorrano, 2016). Specific deletion in astrocytes was achieved by crossing Mfn2 floxed mice (Lee et al., 2012) with the inducible hGFAP-CreER x mitoYFP floxed-stop mouse line (hereafter defined as $Mfn2^{cKO}$ mice). Few weeks after tamoxifen-mediated recombination, MFN2 protein depletion was validated via mass spectrometry analysis of

astrocytes acutely isolated from mouse cortices via magnetic cell separation (MACS) (Figure 3B). In contrast to classic astrocytic markers (i.e., GLAST, GLT-1, ALDH1L1 and AQP4) or other reference mitochondrial proteins (OPA1 and TOMM40), MFN2 was markedly downregulated (Figure 3B). Transmission electron microscopy (TEM) of microvasculature cross-sections revealed fewer and circular mitochondria of significant size in the end-feet of $Mfn2^{cKO}$ astrocytes, in net contrast to $Mfn2^{WT}$ samples, in which elongated and branched morphologies were observed lining the basal lamina (Figure 3C-D). Furthermore, $Mfn2^{cKO}$ mitochondria were less enriched in ER contact sites despite the nearby presence of abundant ER membranes (Figure 3C-D). Notably, deletion of *Mfn2* in astrocytes did not visibly affect mitochondrial cristae morphology within the examined time frame (4 weeks post-tamoxifen treatment) (Figure 3C). Together, these results indicate that conditional deletion of *Mfn2* in adult astrocytes *in vivo* leads to ultrastructural morphological changes of their mitochondria and a concomitant reduction in the extent of mitochondria-ER contact sites within the end-feet.

To gain insights into the potential metabolic changes underpinning lack of MFN2 in astrocytes reacting to injury, we performed a label-free proteomic analysis of astrocytes isolated from injured cortices (4 weeks post-SW) by fluorescence-activated cell sorting (FACS) (Figure 4A and Supp Figure 3A). Inspection of mitochondrial respiratory chain complexes revealed partial but significant changes for several subunits (in particular for complexes I, III, IV and V) in $Mfn2^{cKO}$ astrocytes as compared to controls or even to $Mfn1^{cKO}$ astrocytes, in which changes were less pronounced (Figure 4B). This was corroborated by Ingenuity Pathway Analysis of our dataset, which disclosed the Oxidative Phosphorylation pathway among the $Mfn2^{cKO}$-specific, down-regulated hits in our samples (Supp Figure 3B). Interestingly, expression of tricarboxylic acid (TCA) cycle and associated enzymes showed a general up-regulation both in $Mfn2^{cKO}$ and $Mfn1^{cKO}$ astrocytes (Supp Figure 3C). This was mirrored by the upregulation of several other pathways converging onto the catabolism of amino acids and their derivatives (Supp Figure 3B), which has emerged as a metabolic hallmark of mitochondrial dysfunction also in other cell types (Chen et al., 2018). Likewise, upregulation of AMPK signalling, glycolytic enzymes as well as cholesterol and stearate biosynthesis appeared to be pronounced in both $Mfn2^{cKO}$ and $Mfn1^{cKO}$ astrocytes (Supp

Figure 3B), presumably reflecting a general rewiring of cellular energy metabolism in reactive astrocytes following disruption of Mitofusins (Herzig and Shaw, 2018; Pfrieger and Ungerer, 2011; Wasilewski et al., 2012). Analysis of proteins associated with mitochondrial stress responses revealed that only few of them were significantly up-regulated in $Mfn2^{cKO}$ astrocytes (Supp Figure 3D), suggesting that absence of MFN2 brings about a minor mitochondrial stress on top of potential changes induced by injury itself. Interestingly, upregulation of Wnt/β-catenin signalling, Insulin Receptor signalling as well as of two other pathways (Methylmalonyl and 2-oxobutanoate Degradation) sharing key enzymes (PCCA, PCCB and MUT) important for anaplerotic replenishment of TCA intermediates (Wongkittichote et al., 2017) were specific for $Mfn2^{cKO}$ astrocytes (Supp Figure 3B). Intriguingly, a Calcium Transport pathway was also selectively upregulated in $Mfn2^{cKO}$ astrocytes. In particular, analysis of proteins known to regulate Ca^{2+} influx/efflux through the mitochondrial, ER and plasma membranes revealed differential yet pronounced changes, with a clear trend towards elevated expression of Ca^{2+} channels and transporters in mitochondrial as well as plasma membranes specifically in $Mfn2^{cKO}$ astrocytes (Figure 4C). These data suggest – but do not prove yet – that significant changes in metabolic signalling pathways are induced in reactive astrocytes lacking MFN2.

We next asked the question whether *Mfn2* deletion in astrocytes would be sufficient to prevent mitochondrial network remodeling in response to acute injury. Histological examination of cortical sections derived from lesioned $Mfn2^{cKO}$ animals revealed no overt abnormalities in the extent of GFAP immunoreactivity within the area surrounding the lesion track at 7 days post-SW (Figure 4D). At the single-cell level, however, mitochondrial network morphology appeared significantly affected even in uninjured conditions when compared to control astrocytes (Supp Figure 4A). Besides obvious heterogeneity in the overall mitochondrial population, mitochondria appeared fragmented throughout astrocytic territories, including the end-feet, confirming loss of MFN2 and the consequent lack of mitochondrial fusion dynamics starting as soon as one week after tamoxifen-induced recombination. Interestingly, conditional deletion of MFN1 resulted in somewhat less pronounced morphological changes (Supp Figure 4A), suggesting either differences in the relative expression levels of the two mitofusins or potential compensatory

changes in the expression levels of MFN2 following *Mfn1* deletion, as previously reported for other tissues (Kulkarni et al., 2016). Single-astrocyte time-course analysis of mitochondrial morphology revealed that both Mfn2^{cKO} and Mfn1^{cKO} retained the capability to undergo further fragmentation following SW (Figure 4E). In particular, by 7 days post-SW, i.e. at the peak of fragmentation in control astrocytes, the overall proportion of fragmented versus tubular mitochondria appeared almost indistinguishable between all examined groups (Figure 4E). However, while control and Mfn1^{cKO} astrocytes gradually and efficiently reformed a tubular network by 28 days post-SW, Mfn2^{cKO} astrocytes lacked this ability and were thereafter left with visibly fragmented and swollen mitochondria (Figure 4E-F). Importantly, perivascular mitochondrial clustering induced by injury was significantly impaired in Mfn2^{cKO} astrocytes proximal to the lesion site, in contrast to control and Mfn1^{cKO} astrocytes, in which the extent of mitoYFP signal essentially doubled (Figure 4G-H, Supp Figure 4B). Altogether, these results indicate that local perivascular accumulation of astrocytic mitochondria can be prevented by acute *Mfn2* deletion and thus, that this process requires mitochondrial fusion dynamics.

Lack of MFN2 dampens astrocytic mitochondrial Ca^{2+} uptake and leads to abnormal perivascular Ca^{2+} transients after SW-injury *in vivo*

The absence of a clear perivascular mitochondrial clustering in reactive Mfn2^{cKO} astrocytes provides an opportunity for investigating potential functional consequences confined to this cellular compartment. As astrocytes are characterized by a rich variety of spontaneous Ca^{2+} transients which are central in regulating several astrocytic functions including neurovascular coupling (Bazargani and Attwell, 2016; Volterra et al., 2014) and given that a Ca^{2+} transport pathway was uniquely up-regulated in Mfn2^{cKO} astrocytes in our proteomic analysis we assessed local Ca^{2+} dynamics as a proxy to identify metabolic changes in astrocytic end-feet under resting or reactive conditions. We first evaluated the extent of mitochondrial Ca^{2+} uptake by stereotactically delivering an astrocyte-specific AAV expressing the calcium indicator GCaMP6f targeted to the mitochondrial matrix (mitoGCaMP6) in the cerebral cortex of Mfn2^{cKO} or control littermates, and concurrently inflicted a unilateral SW lesion in the injected area (Figure 5A). We then conducted 2-photon laser

scanning microscopy (2PLSM) at 7 or 28 days after SW in freshly prepared brain slices. Imaging was carried out in sessions of 3 minutes each, which corresponded to a time window during which mitochondrial movement or fusion-fission dynamics - as examined via photoactivatable mito-GFP experiments in comparable settings - were negligible (Supp Figure 5A-C), thus allowing a reliable quantification of local relative changes in mitoGCaMP6 signal. We also developed a dedicated algorithm (which we termed AstroSparks, see methods) permitting a semi-automated identification and quantification of spontaneous mitochondrial Ca^{2+} transients, including their activity, frequency, amplitude and duration (Figure 5B). This allowed us to reveal that, in resting astrocytes, perivascular mitochondria were intrinsically more active but displayed a lower amplitude in their Ca^{2+} transients than mitochondria localized in branches and branchlets (Figure 5C-D). Comparison with $Mfn2^{cKO}$ astrocytes under uninjured conditions (Figure 5E) revealed that these possess an intrinsically much lower mitochondrial Ca^{2+} activity within their end-feet (46.6% active ROIs of all ROIs per cell) as compared to $Mfn2^{WT}$ astrocytes (68.2 % active ROIs of all ROIs per cell) (Figure 5F). Interestingly, following SW-injury $Mfn2^{WT}$ astrocytes displayed a peculiar pattern in their mitochondrial Ca^{2+} uptake dynamics that mirrored the morphological changes in mitochondrial network architecture described in Figure 2E: by 7 days (i.e. the peak of mitochondrial fragmentation) the extent of active mitochondria was visibly reduced (55.3 % of all ROIs per cell), whereas by 28 days (the time when mitochondrial tubular morphology had been re-established) this percentage had reverted to levels comparable to uninjured conditions (62.8 %) (Figure 5F). Likewise, most of the other parameters pertaining to Ca^{2+} uptake dynamics, particularly the frequency of the Ca^{2+} events per mitochondrion and their duration, also followed a reversible pattern over time in $Mfn2^{WT}$ astrocytes (Figure 5G). In contrast, analysis of $Mfn2^{cKO}$ astrocytes revealed that mitochondria in these cells are virtually unresponsive to injury-induced changes of Ca^{2+} uptake all through the analysed times (Figure 5F-G). In particular, the values of frequency, amplitude and duration of Ca^{2+} transients were not only already affected in absence of any SW-injury, but also compared rather well with the 7-day-SW time-point of the $Mfn2^{WT}$ group (Figure 5G), suggesting that primary alterations in mitochondrial network morphology (i.e. towards

fragmentation) and ER-tethering *per se* are, at least in part, responsible for the changes in mitochondrial Ca^{2+} uptake observed here.

Analysis of slices containing cytoGCaMP6-expressing astrocytes revealed plain differences with regard to Ca^{2+} transients taking place in the cytosol as compared to mitochondria (Figure 5H and Supp Figure 5D-E). In fact, cytosolic transients in uninjured $Mfn2^{WT}$ astrocytes were markedly shorter in duration and, on average, higher in frequency than mitochondrial ones (Figure 5H and Supp Figure 5E-F), consistent with a role played by mitochondria in rapidly buffering Ca^{2+} ions following cytosolic influx (Rizzuto et al., 2012). SW-injury in cytoGCaMP6-expressing $Mfn2^{WT}$ astrocytes significantly modified perivascular cytosolic transients at 7 days (Supp Figure 5F), yet these changes were not fully reversed by 28 days post-SW, suggesting the emergence of long-lasting alterations in the expression of membrane Ca^{2+} transporters and/or handling mechanisms that may persist up to 1 month after injury. Notably, cytosolic transients were significantly altered upon conditional deletion of *Mfn2* (Supp Figure 5E-F) and culminated in an exaggerated Ca^{2+} activity (i.e., frequency and amplitude of events) by 28 days post-SW (Supp Figure 5F), thus validating our proteomic data (Figure 4C). Interestingly, similar changes in Ca^{2+} activity were also observed in astrocyte branches (Supp Figure 5G), suggesting that lack of MFN2 affected mitochondrial and cytosolic Ca^{2+} frequency dynamics to an overall comparable extent in both astrocytic territories.

While slice imaging allowed us to identify the overall changes in astrocytic mitochondrial and cytosolic Ca^{2+} activity following SW-injury, it precluded the possibility to examine in detail the regionalized Ca^{2+} dynamics within an intact neurovascular unit. To circumvent this caveat, we performed 2PLSM of $Mfn2^{cKO}$ astrocytes in anesthetized animals *in vivo* following cranial window implantation and concurrent vasculature labelling with dextran-red (Figure 5I). For these experiments we utilized the inducible reporter line GCaMP3 floxed-stop (Zariwala et al., 2012) to replace the mitoYFP reporter in our $Mfn2^{cKO}$ mice, thus allowing for a systematic analysis of subcellular changes in cytosolic Ca^{2+} activity without the need to inject any AAV. In particular, dextran labelling allowed us to unambiguously identify perivascular end-feet in GCaMP3-expressing astrocytes *in vivo*, and by exclusion the main branches and branchlets (Figure 5J).

Analysis of Ca^{2+} frequency in this setting confirmed that $Mfn2^{WT}$ astrocytes undergo major alterations in response to SW-injury peaking at 7 days and persisting up to 28 days (Figure 5L and Supp Fig 5G). However, by this time *Mfn2* deletion led to an abnormal frequency of Ca^{2+} events which resulted in much higher rates of perivascular transients (0.64±0.03 events/min/domain in $Mfn2^{cKO}$ astrocytes vs 0.46±0.01 events/min/domain in controls) (Figure 5K-L). While this phenotype was again apparent both in end-feet and branches (Supp Figure 5G), analysis of spatial spreading of Ca^{2+} transients within astrocytic territories revealed that prominent and enduring changes (i.e. broader transients) up to 28 days post-SW were a unique feature of perivascular compartments in astrocytes lacking MFN2 (4.98±0.67 μm^2 in $Mfn2^{cKO}$ vs 3.25±0.33 μm^2 in $Mfn2^{WT}$) (Figure 5M). This hallmark was masked at 7 days post-SW, i.e. a time when control astrocytes also showed broader transients presumably due to their conspicuous mitochondrial fragmentation and reduced mitochondrial Ca^{2+} uptake (Figure 5G), yet this specificity for the end-feet suggests that injury-induced accumulation of mitochondria at these precise sites helps to demarcate a region of distinctive Ca^{2+} signalling and metabolic supply.

Astrocyte mitochondrial fusion dynamics are required for vascular repair following injury

We next asked if the perivascular changes in mitochondrial clustering and metabolic activity exhibited by $Mfn2^{cKO}$ astrocytes may have direct consequences for vascular repair or BBB integrity. For this purpose, SW-injured mice were intravenously infused with dextran-red shortly before sacrifice and their cortices processed for clearing and 2PLSM to obtain a complete overview of the functional vascular network (Figure 6A). Top views of the first 600μm deep into the cortex revealed that uninjured hemispheres were virtually undistinguishable among $Mfn2^{cKO}$ and $Mfn2^{WT}$ mice, showing comparable density and integrity of the labelled vasculature (Figure 6B). By 7 days post-SW, however, $Mfn2^{cKO}$ mice showed a more conspicuous extravasation of dextran and a pronounced rarefication of the vasculature within the lesion core. At this time, the lesion track was still visible also in $Mfn2^{WT}$ mice, however the vascular density appeared higher than in $Mfn2^{cKO}$ mice (Figure 6B). By 28 days, the observed rarefication in control mice appeared virtually resolved at the location where the previous injury had been inflicted. In contrast, the lesion core in $Mfn2^{cKO}$

mice retained much of the alterations identified at 7 days, suggesting that functional repair of the microvasculature was significantly affected. To gain insights into the actual structural density of microvessels in these settings, we visually inspected CD31 immunoreactivity (i.e. a marker for endothelial cells) in brain sections derived from injured Mfn2^{cKO} mice and control littermates expressing a tdTomato reporter in astrocytes. Interestingly, in contrast to dextran labelling the CD31 staining revealed a pronounced sprouting of vessels in the lesion area of control mice by 7 days post-SW (Supp Fig 6E), indicating that these may be neoformed vessels that did not yet fully connect with the pre-existing vascular network. The extent of vascular remodeling in Mfn2^{cKO} samples, on the other hand, appeared more contained despite abundance of tdTomato+ astrocytes (Supp Fig 6E). Importantly, quantification of astrocyte numbers and inspection of perivascular end-feet in these tdTomato-expressing Mfn2^{cKO} mice revealed no overt changes as compared to Mfn2^{WT} mice (Supp Fig 6E-G), ruling out possible additional effects due to astrocyte degeneration or prominent changes in their proliferative capacity.

To systematically quantify the extent of functional vascularization in the injured area, we optimized a filament tracing analysis utilizing dextran labelling as a mask signal for our volumetric reconstructions (Figure 6C and Supp Fig 7A), and performed a time-course analysis in Mfn2^{WT} and Mfn2^{cKO} mice including 3, 7 and 28 days post-SW. At the earliest analysed time (3 days), we identified a similar reduction in the density of branch points as well as total length and fractional vascular volume of the network surrounding the injury track (i.e., within a fixed total volume of about 0.2 mm^3) as compared to uninjured conditions (Figure 6D). Yet, while by 7 days the Mfn2^{WT} group showed a partial recovery of these parameters (in particular branch points) which became conspicuous by 28 days, Mfn2^{cKO} injured cortices failed in undergoing significant improvements (Figure 6D). Interestingly, analysis of Mfn1^{cKO} mice performed at 7 days post-injury (i.e. the earliest time showing clear differences in Mfn2^{cKO} mice) did not reveal striking dissimilarities compared to control SW-injured mice for any of the examined vascular parameters (Figure 6E and Supp Fig 6A), in line with the fact that disruption of MFN1 expression alone did not prevent perivascular clustering of mitochondria (Figure 4G-H). To understand if the vascular phenotype identified in Mfn2^{cKO} mice was MFN2-specific, we performed the same experiments in a third conditional

mouse model in which mitochondrial fusion was also visibly impaired. We utilized astrocyte-specific Yme1l^{cKO} mice, in which deletion of the mitochondrial *i*-AAA protease *Yme1l* disrupts the proteolytic processing of the inner membrane GTPase OPA1, leading to a marked mitochondrial fragmentation in cells (Anand et al., 2014) but only minor and late-onset OXPHOS deficiency (Sprenger et al., 2019). Similar to Mfn2^{cKO} astrocytes, Yme1l^{cKO} astrocytes displayed a conspicuous fragmentation of their mitochondrial network *in vivo* (Supp Fig 6B). Furthermore, SW-injury failed in eliciting a visible perivascular mitochondrial enrichment in these astrocytes (Supp Fig 6C-D). Strikingly, vascular recovery in injured Yme1l^{cKO} cortices was also significantly impaired (Figure 6E and Supp Fig 6A), indicating that this phenotype is not strictly MFN2-dependent. Rather, these results indicate that lack of mitochondrial fusion dynamics prevents perivascular clustering of mitochondria in injury-induced reactive astrocytes, compromising the repair of the vascular network.

Forced enrichment of mitochondria in perivascular end-feet rescues microvasculature repair in absence of mitochondrial fusion

We next asked whether perivascular accumulation of mitochondria following injury and BBB disruption may be sufficient to establish a local metabolic domain and sustain vascular repair. To answer this question, we took advantage of a previously validated strategy to forcefully anchor mitochondria to ER membranes using a genetically-encoded synthetic linker (Csordas et al., 2006) that we expressed in Mfn2^{cKO} mice via an astrocyte-specific AAV (pAAV-hGfaABC$_1$D-OMM-mRFP-ER) (Figure 7A). We reasoned that, since the overall extent of perivascular astrocytic ER membranes appeared to large degree conserved in absence of MFN2 (Figure 3C), anchoring mitochondria to ER tubules prior tamoxifen treatment (and *Mfn2* deletion) by means of this irreversible linker could progressively enhance and stabilize the extent of perivascular mitochondria irrespective of subsequent changes in morphology and fission-fusion dynamics. The construct encoding for this linker contains a monomeric RFP fused on the one side to the outer mitochondrial membrane (OMM)-targeting sequence of mAKAP1 and on the other to the ER membrane-targeting sequence of yUBC6 (Figure 7B) (Csordas et al., 2006). Its expression in different systems

markedly expands the interface area between mitochondria and ER, resulting in mRFP labelling of the OMM (Arruda et al., 2014; Csordas et al., 2006; Csordas et al., 2010). Few weeks after intracortical delivery of this AAV-linker (or its AAV control lacking the ER targeting sequence), mice were treated with tamoxifen to induce *Mfn2* deletion (Figure 7A) followed by SW-injury and mitochondrial network analysis. At the single-astrocyte level, the overall morphology of the mitochondrial network was not significantly affected, with most mitochondria still appearing visibly fragmented even in absence of injury (Figure 7B), as expected in astrocytes lacking mitochondrial fusion. However, we noticed that the amount of mRFP+ mitochondria decorating vessel cross-sections was visibly increased in astrocytes transduced with the AAV-linker as compared to controls both in resting and injured conditions (Figure 7B-D). To understand if this manipulation also modified the metabolic environment in perivascular end-feet, we introduced a cassette encoding for mitoGCamp6f in the OMM-mRFP-ER construct (Supp Figure 7B-C). Analysis of mitoGCamp6f in resting $Mfn2^{cKO}$ astrocytes revealed that AAV-linker transduction modified the extent of mitochondrial Ca^{2+} uptake by increasing both the percentage of active mitochondria and their frequency dynamics (Figure 7E and Supp Figure 7D-E) to levels almost comparable to $Mfn2^{WT}$ astrocytes (Figure 5F-G), indicating that this forced tethering was sufficient to enhance MAM-dependent Ca^{2+} uptake in $Mfn2^{cKO}$ astrocytes.

We next analysed the extent of vasculature remodeling induced by SW-injury in the area subjected to AAV transduction. Visual inspection of CD31 immunoreactivity confirmed that non-transduced $Mfn2^{cKO}$ cortices were characterized by thinner and less branched vessels throughout the injured area (Figure 7F and H). Importantly, while injection of the AAV-ctrl did not overtly change the extent of CD31 immunostaining by 7 days post-SW, AAV-linker expression significantly enhanced vascular density to levels almost indistinguishable from those of $Mfn2^{WT}$ mice (Figure 7G and H), and in particular it did improve the thickness and sprouting of vessels within the injured tissue. Together, these results indicate that, within the examine time frames, manipulation of perivascular mitochondrial clustering and mitochondrial-ER tethering in astrocytic end-feet can be exploited to compensate for lack of mitochondrial fusion and facilitate vasculature repair after injury.

Discussion

We have shown that a profound reorganization of the mitochondrial network in astrocytes responding to acute injury underlies their ability to create a spatially defined mitochondrial-enriched domain in perivascular end-feet. Astroglial end-feet appear to be naturally enriched in elaborated mitochondrial morphologies and bundles of ER tubules, which is in line with recent observations (Mathiisen et al., 2010; Moss et al., 2016), yet during the first week that follows injury these cellular sites experience a further accumulation of mitochondria as a result of coordinated fusion-fission dynamics. While mitochondrial biogenesis or trafficking are also likely to contribute in this process, mitochondrial fusion in particular was required to promote the formation of this localized clustering as deletion of *Mfn2* not only prevented this response, but also significantly altered local "metabolic" signalling, as revealed by Ca^{2+} imaging experiments. Importantly, the extent of mitochondrial accumulation in astrocytic end-feet had direct consequences for microvasculature repair: while depletion of mitochondria impaired vascular network recovery in lesioned cortices, mitochondrial enrichment had opposite results and rescued vascular density even in absence of mitochondrial fusion. This finding is reminiscent of an equally enhanced accumulation of mitochondria to new axonal sprouts following axotomy experiments, a process which has implications for axon regeneration (Han et al., 2016; Mar et al., 2014; Misgeld et al., 2007). Along this line, our data support the notion that mitochondrial enrichment in astrocytic end-feet does not simply identify a general trait of cellular reactivity but rather a mechanism that is triggered to ensure the formation of an active metabolic compartment with direct implications for vascular remodeling.

Our experiments performed on astrocyte-specific $Mfn2^{cKO}$ mice were specifically designed to manipulate the mitochondrial network shortly (~2 weeks) before inflicting the SW-injury, thereby allowing mice to develop and reach adulthood with normal MFN2 expression until the first day of tamoxifen treatment. This time was sufficient to elicit a significant drop in MFN2 protein expression *in vivo*, which was mirrored by evident changes in mitochondrial morphology and ultrastructure. This indicates that mitofusins have a relatively rapid turnover in astrocytes and allowed us to focus on the acute effects resulting from lack of mitochondrial fusion. While this may explain the

seemingly intact cristae morphology observed in Mfn2^{cKO} astrocytes, in contrast to developmental knockout studies (Chen et al., 2007; Lee et al., 2012), it is of particular interest the fact that morphological changes towards circular and fragmented mitochondria were accompanied by a reduction in the extent of MAM domains with the ER in astrocytic end-feet. In cell lines, MFN2 has been repeatedly reported to regulate the extent of tethering between these two organelles, with a pro-tethering (de Brito and Scorrano, 2008; Naon et al., 2016) rather than an anti-tethering activity (Filadi et al., 2015) being validated also in other *in vivo* studies (Luchsinger et al., 2016; Schneeberger et al., 2013). Here, a reduction in MAMs and an increased mitochondria-ER distance in astrocytes supports a similar pro-tethering role of MFN2. However, we cannot entirely exclude that these may develop as secondary effects due to morphological changes of the mitochondrial network in perivascular end-feet.

One of the key findings of our study is the observation that the enrichment of mitochondria within end-feet contributes to shape the local environment surrounding microvessels *in vivo* and *ex vivo*, as revealed by Ca^{2+}-imaging experiments performed with the GCamp6f sensor. Interestingly, our analysis revealed that the end-foot is characterized by distinctive mitochondrial Ca^{2+} uptake dynamics when compared to branches and branchlets of the same cell, which may be justified by the enrichment in mitochondria-ER contact sites precisely in perivascular processes. Astrocytes possess a remarkably complex Ca^{2+} activity on account of their highly ramified morphology (Bindocci et al., 2017; Shigetomi et al., 2016) and changes in the pattern of spontaneous and stimulus-induced Ca^{2+} transients have been shown to associate with synaptic transmission and vascular tone (Bindocci et al., 2017; Tran et al., 2018; Wang et al., 2006). Besides the ER, mitochondria are also well known for being integral components of Ca^{2+} signalling in cells given their significant Ca^{2+} buffering capacity which is primarily regulated by the mitochondrial calcium uniporter (MCU) complex (Baughman et al., 2011; De Stefani et al., 2011). Calcium uptake can modify mitochondrial bioenergetics (Giorgi et al., 2018), but also it can modulate the magnitude and spread of cytosolic Ca^{2+} transients and thus have important effects on key signalling events in cells, including astrocytes *in vitro* (Jackson and Robinson, 2015; Li et al., 2014; O'Donnell et al., 2016; Parnis et al., 2013; Parpura et al., 2011; Reyes and Parpura, 2008; Stephen et al., 2015)

and *in vivo* (Agarwal et al., 2017). As MCU exhibits low Ca^{2+}affinity, mitochondrial Ca^{2+} influx predominantly occurs at sites of elevated Ca^{2+} concentrations, i.e. mitochondria-plasma membrane and mitochondria-ER tethering domains (Hayashi et al., 2009; Rizzuto et al., 2012). Intriguingly, manipulation of MFN2 expression levels has been shown to alter mitochondrial Ca^{2+} buffering capacity in cells as a consequence of its regulatory role on mitochondria-ER tethering domains (de Brito and Scorrano, 2008; Filadi et al., 2015; Luchsinger et al., 2016; Naon et al., 2016). Consistent with these earlier reports, here we find that a marked dampening of mitochondrial Ca^{2+} activity in $Mfn2^{cKO}$ astrocytes *in situ* renders these cells virtually insensitive to the changes in mitochondrial Ca^{2+} dynamics induced by injury. Importantly, while this impaired mitochondrial Ca^{2+} uptake is likely to impact local bioenergetics, it also translates into long-term alterations in cytosolic Ca^{2+} activity which, at the level of the end-feet, manifest as Ca^{2+} transients wider and more frequent than those observed in control end-feet.

Unexpectedly, we found that abrogation of astrocyte mitochondrial fusion dynamics was sufficient to impair vascular network recovery after injury. While we propose this effect to be primarily mediated by a faulty metabolic domain at the gliovascular interface, at this stage we can only speculate what the exact signalling might be that facilitates vasculature repair in control conditions. Interestingly, MFN2-mediated signalling has been implicated in regulating cell proliferation in vascular smooth muscle cells (Chen et al., 2004), however here we did not find overt changes in astrocyte numbers in our system. Also, the fact that astrocytes can sustain a glycolytic metabolism for extended periods of time under resting conditions (Supplie et al., 2017) argues against a primary role of OXPHOS in this regard. Nonetheless, accumulating evidence suggests that severe astrocytic OXPHOS dysfunction may become a relevant aspect in settings of injury (Fiebig et al., 2019; Ignatenko et al., 2018). Yet, induction of mitochondrial enrichment via AAV-linker expression alone in $Mfn2^{cKO}$ mice was sufficient to restore a normal vascular density, despite partial astrocytic OXPHOS dysfunction. Also, while astrocyte-specific *Yme1l* deletion reproduced most of the mitochondrial and vascular phenotypes identified in $Mfn2^{cKO}$ mice, CNS-specific *Yme1l* knock-out mice show only a mild OXPHOS deficiency (Sprenger et al., 2019), suggesting that alterations in astrocyte mitochondrial respiration *per se* may not be the leading

cause for the lack of vascular repair. One intriguing possibility, however, is that this close apposition to the BBB of a dense supply of mitochondria in control astrocytes may favour either the local release of specific signalling molecules or contribute to generate locally a chronic metabolic environment (Al-Mehdi et al., 2012; Lopez-Fabuel et al., 2016), which may act non cell-autonomously in assisting the angiogenic response during the days that follow the initial insult (Wong et al., 2017). Alternatively, a directed supply of key astrocytic biosynthetic intermediates, as those generated by the TCA cycle (Lovatt et al., 2007), or ATP itself may contribute to fuel the remodeling of the gliovascular interface (Boulay et al., 2017; Rangaraju et al., 2019) as well as restore perivascular barrier (Voskuhl et al., 2009) or clearance functions, in particular of toxic metabolic by-products (Iliff et al., 2012). Ultimately, a combination of multiple factors, possibly converging onto the localized release of pro-angiogenic signalling molecules (Sweeney et al., 2016), are likely to participate in regulating astrocyte-mediated vascular remodeling following injury.

In conclusion, our study provides insights into the metabolic changes experienced by astrocytes during their response to injury and BBB disruption, but also it identifies an important mechanism through which these cells may directly contribute to vascular remodeling in the damaged brain. Successful molecular dissection of the metabolic pathways playing a role in this process may therefore hold promise for therapeutic interventions to ameliorate tissue repair.

Acknowledgements

We thank N.G. Larsson for providing mitoYFP floxed-stop, Mfn1 floxed and Mfn2 floxed mice. T. Langer for Yme1l floxed mice and for insightful comments. M. Götz and F. Kirchhoff for Glast::CreERT2 mice. L. Uhrbom and E. Holland for hGFAP-TVA mice. E.L. Snapp for ER-targeted probes. G. Hajnoczky for synthetic linkers. N. Toni for advices on EM. I. Atanassov for support with IPA analysis. B. Fernando and T. Öztürk for excellent technical assistance. J. Matutat, G. Piper, D. Schneider and the other members of the CECAD in vivo facility for excellent assistance. G. Wani, S. Wendler, K. Ndoci and T. Eriksson for general lab support and discussions. All members of the CECAD imaging facility for assistance with microscopes and software. The team of the CECAD proteomics core facility for technical assistance. This work was supported by the Deutsche Forschungsgemeinschaft (SFB1218 A07), European Research Council (ERC-StG-2015, grant number 67844), Köln Fortune and UoC Advanced Postdoc Grant to M.B. A.S. is supported by the Deutsche Forschungsgemeinschaft (SFB1218 Z03). E.M. is recipient of an Advanced Postdoc Grant (Deutsche Forschungsgemeinschaft, SFB1218).

Author Contributions

J.G. performed and analysed most of the experiments. P.P. developed the custom algorithm for Ca^{2+} analysis. V.S. and M.J. generated and validated AAVs. E.E., H.M.J. and A.S. contributed to experiments. K.F.D. and C.K. supported with cell sorting. A.G. and K.K.C. provided reagents. C.F. performed mass-spec and initial analysis. E.M. contributed to proteomic analysis. J.G. and M.B. prepared figures. E.M. and M.B. developed the concept. M.B. designed experiments, analysed data and wrote the paper. All authors revised the manuscript.

Author Information

The authors declare no competing financial interests.

Figure legends

Figure 1. Astrocytic end-feet are enriched in mitochondria-ER contact sites. (A) Experimental design used to express organelle-targeted fluorescent sensors in astrocytes *in vivo*. **(B)** Example of a cortical astrocyte co-transduced with ER-GFP and mitoRFP viruses. Yellow arrowheads point to the end-feet. Bar, 10 µm. **(C)** Magnifications of the astrocyte shown in B. Yellow arrowheads point to bundles of elongated mitochondria. Bar, 5 µm. **(D-E)** Examples of astrocytes transduced with ER-GFP (D) or mitoYFP (E) wrapping around dextran-labeled vessels. Insets show zooms of the perivascular end-foot. Side panels show a 3D rendering of the same astrocytes. Bars, 10 and 20 µm. **(F)** EM picture of a vessel cross-section showing the astrocytic end-foot (segmented black line) and its organelles (mitochondria: yellow; ER: red; contact sites: blue). The inset shows mitochondria-ER contact sites lining the basal lamina. Bars, 2 and 1 µm. **(G)** EM picture of perisynaptic astrocytic processes and their organelles. Bar, 2 µm. **(H)** Quantification of mitochondrial parameters in branches (n= 15 vessel cross-sections from 2 mice) and end-feet (n= 26 vessel cross-sections from 2 mice; nonparametric Mann-Whitney t-test). ***, $p< 0.001$. PC: pericyte; EC: endothelial cell; BL: basal lamina.

Figure 2. Dynamic remodeling of astrocyte mitochondrial networks following injury. (A) Experimental design for examining the mitochondrial network in astrocytes *in vivo*. **(B)** Example of an hGFAP::CreERT x R26$^{LSL\text{-}mitoYFP}$ mouse at 7 days after cortical SW-injury. The inset shows CD45+ leukocytes in the lesion core. Bar, 100 µm. **(C)** Surface rendering of mitochondrial networks in reactive astrocytes located in the lesion core or scar regions. Yellow arrowheads point to the soma. Insets show immunoreactivity for GFAP. Zooms depict the predominant network morphology. Bar, 15 µm. **(D)** Density plots depicting the morphological heterogeneity of the mitochondrial population in individual astrocytes under resting (Ctrl) or reactive conditions (SW 7days). The proportion of fragmented mitochondria based on threshold values for mitochondrial sphericity (0.8) and length (1 µm) is highlighted. **(E)** Time-course analysis of mitochondrial fragmentation quantified as in E (n≥ 3 mice/time point, with 8-15 astrocytes/mouse; one-way ANOVA followed by Dunnett's post-hoc test). **(F)** Volume reconstruction of mitoYFP+ astrocytes

(arrowheads) surrounding dextran-labelled vessels at 7 days post-SW. A single-stack is shown. Bar, 25 µm. **(G)** Examples of vessel cross-sections showing perivascular astrocytic mitoYFP in control and injured conditions. Bar, 10 µm. **(H)** Quantification of perivascular mitoYFP density displayed as area fraction (n≥ 30 vessels obtained from 3 mice/time-point; nonparametric Kruskal-Wallis test). **(I)** Experimental design for analyzing the astrocytic ER. **(J)** 3D example of an astrocyte expressing ER-GFP (signal density shown in pseudocolors). Bars, 10 and 5 µm. **(K)** Quantification of the ER-GFP perivascular *g-ratio* at the indicated time-points (n≥ 35 vessels obtained from 2 mice/time-point; nonparametric Kruskal-Wallis test). **, $p < 0.01$, ***, $p < 0.001$.

Figure 3. *Mfn2* deletion affects astrocytic mitochondria-ER tethering domains. (A) Proposed model showing the extent of mitochondrial remodeling taking place in astrocytic end-feet during injury and the expected phenotype following *Mfn2* deletion. **(B)** Experimental design for validating *Mfn2* knock-out in astrocytes by MACS enrichment and proteomic analysis. The plot shows MFN2 protein abundance in $Mfn2^{cKO}$ samples compared to other mitochondrial and classic astrocytic markers (n= 4 $Mfn2^{cKO}$ mice and 3 $Mfn2^{WT}$ mice). **(C)** EM pictures of astrocytic end-feet in $Mfn2^{WT}$ and $Mfn2^{cKO}$ mice at 4 weeks post-tamoxifen treatment. Mitochondria and ER contact sites are highlighted in different colors. Right panels depict zooms of mitochondrial cristae. EC: endothelial cell; BL: basal lamina. Bars, 1 µm and 200 nm. **(D)** Quantification of the indicated ultrastructural parameters in $Mfn2^{WT}$ (n= 85 vessel cross-sections from 4 mice) and $Mfn2^{cKO}$ perivascular end-feet (n= 145 vessel cross-sections from 3 mice; non-parametric Mann-Whitney t-test). ***, $p < 0.001$.

Figure 4. Astrocyte-specific deletion of *Mfn2* prevents perivascular mitochondrial clustering. (A) Schematic illustrating the experimental protocol used for astrocyte isolation via anti-ACSA staining and FACS followed by mass spectrometry and data analysis. **(B-C)** Heat maps of normalized LFQ (label-free quantification) intensities of detected (B) OXPHOS complex subunits and (C) proteins regulating Ca^{2+} transport (across the membrane of the indicated organelles) color-coded according to their fold increase against the median of the control values (n= 4 $Mfn2^{cKO}$ mice, 4 $Mfn1^{cKO}$ mice and 3 Ctrl mice). Significant changes ($-\log_{10}$ of the *p*-value ≥1.3) are indicated with

an asterisk. **(D)** Example of cortical SW-injury in Mfn2^{cKO} mice at 7 days. The inset shows CD45+ leukocytes within the lesion core. Bar, 100 µm. **(E)** Time-course analysis of mitochondrial fragmentation in Mfn2^{cKO} and Mfn1^{cKO} astrocytes (n≥ 3 mice/time point, 8-15 astrocytes/mouse; two-way ANOVA followed by Tukey's post-hoc test). **(F)** Examples of mitochondrial morphologies in astrocytic processes (arrowheads point to soma) proximal to the lesion site at 28 days post-SW. Insets show immunoreactivity for GFAP. Bar, 20 µm. **(G)** Top view projections (100 µm deep) of Mfn2^{cKO} and Mfn1^{cKO} injured cortices (7 days) following tissue clearing. The injury site is indicated by a yellow dashed line. Middle panels depict a mitoYFP-expressing astrocyte and nearby vessels. Right panels depict the vessel cross-section. Bars, 80, 10 and 10 µm. **(H)** Quantification of astrocytic mitoYFP perivascular density (n≥ 80 vessel sections from 3 mice/condition; the contralateral uninjured sides were utilized as internal controls; one-way ANOVA followed by Holm-Sidak's post-hoc test). *, $p < 0.05$, **, $p < 0.01$, ***, $p < 0.001$.

Figure 5. Impaired mitochondrial Ca^{2+} uptake and abnormal cytosolic Ca^{2+} activity in Mfn2^{cKO} astrocytic end-feet. (A) Schematic showing mitoGCaMP6f expression in astrocytes followed by 2PLSM and subsequent AstroSparks analysis. **(B)** Example of a mitoGCaMP6-expressing Mfn2^{WT} astrocyte in brain slice following AstroSparks processing and ROI detection (ROIs in end-feet are depicted in white; soma was excluded). Inset displays cytosolic mCherry (co-expressed with mitoGCaMP6), used to identify the end-feet. Bar, 10 µm. Right panels depicts individual ROI traces and the corresponding raster plot. **(C-D)** Quantification of mitochondrial Ca^{2+} transients in branches and end-feet of uninjured Mfn2^{WT} astrocytes (n= 41-53 cells from 3 mice). **(E)** Example of a mitoGCaMP6-expressing Mfn2^{cKO} astrocyte with corresponding ROI traces and raster plot. Bar, 10 µm. **(F)** Quantification of active mitochondria in Mfn2^{WT} (n= 40-56 cells, 3 mice/condition) and Mfn2^{cKO} (n= 36-73 cells, at least 2 mice/condition) astrocytic end-feet. **(G)** Quantification of frequency, amplitude and duration of mitochondrial Ca^{2+} transients of the astrocytes in **F**. **(H)** Example of mitochondrial and cytosolic Ca^{2+} traces. **(I)** Experimental setting utilized for Ca^{2+} imaging in Mfn2^{cKO} astrocytes *in vivo*. **(J)** Example of a GCaMP3-expressing astrocyte imaged *in vivo* following ROIs detection (excluding the soma). Bar, 20 µm. **(K)** Examples

of ROI traces and corresponding raster plot in Mfn2^{WT} and Mfn2^{cKO} astrocytes by 28 days post-SW. **(L)** Average frequency (end-feet) and **(M)** area of Ca^{2+} transients quantified in Mfn2^{WT} (n= 35-111 cells from at least 2 mice/condition) and Mfn2^{cKO} astrocytes (n= 51-73 cells from at least 2 mice/condition). *, $p < 0.05$, **, $p < 0.01$, ***, $p < 0.001$ (nonparametric Mann-Whitney t-test).

Figure 6. Disruption of astrocyte mitochondrial fusion dynamics affects vascular repair. (A) Experimental protocol used for examining the vascular network following injury. **(B)** Top views of the vascular network in reconstructed portions of Mfn2^{WT} and Mfn2^{cKO} cortices. Arrowheads point to the lesion tracks. Insets depict zooms of the lesioned core region (circled in white). Bar, 200 µm. **(C)** Pipeline used for vasculature quantification via filament tracing. Bar, 30 µm. **(D)** Quantification of branch points, fractional volume and total length of the vascular network in Mfn2^{WT} and Mfn2^{cKO} cortices (n= 3 mice/condition; two-way ANOVA followed by Tukey's post-hoc test). **(E)** Vascular network quantification in Mfn1^{WT} and Yme1l^{cKO} cortices at 7 days post-SW (n= 3-4 mice/condition; one-way ANOVA followed by Tukey's post-hoc test). *, $p < 0.05$, **, $p < 0.01$, ***, $p < 0.001$.

Figure 7. Forced enrichment of mitochondria in perivascular end-feet rescues vascular recovery in injured Mfn2^{cKO} mice. (A) Experimental plan for expressing the artificial mitochondria-ER linker (OMM-mRFP-ER) in Mfn2^{cKO} astrocyte *in vivo*. **(B)** Example of an AAV-linker-expressing Mfn2^{cKO} astrocyte (arrowhead points to the soma) showing mRFP-labelled mitochondria and a nearby vessel. Zooms depict a vessel cross-section. Bar, 10 µm. **(C)** Examples of vessel cross-sections following expression of the AAV-ctrl or AAV-linker in Mfn2^{cKO} astrocytes. Bar, 5 µm. **(D)** Quantification of perivascular mRFP density displayed as area fraction (n≥ 21 vessel sections from 2 mice/condition; one-way ANOVA followed by Tukey's post-hoc test). **(E)** Quantification of mitochondrial Ca^{2+} uptake in Mfn2^{cKO} astrocytes following expression of mitoGCaMP6f in the AAV-ctrl and AAV-linker (n≥ 30 cells from 2 mice/condition; nonparametric Mann-Whitney t-test). **(F)** Examples of vasculature density (CD31+) in Mfn2^{WT} and Mfn2^{cKO} sections at 7 days post-SW (dashed line points to the lesion track). Bar, 80 µm. **(G)** Examples of vasculature density in injured Mfn2^{cKO} cortices transduced with the AAV-Ctrl or AAV-linker. Bar,

80 µm. **(H)** CD31 area fraction in $Mfn2^{WT}$ and $Mfn2^{cKO}$ cortical sections under the indicated conditions (n≥ 3 mice/condition; one-way ANOVA followed by Tukey's post-hoc test). *, $p < 0.05$, **, $p < 0.01$, ***, $p < 0.001$.

References

Agarwal, A., Wu, P.H., Hughes, E.G., Fukaya, M., Tischfield, M.A., Langseth, A.J., Wirtz, D., and Bergles, D.E. (2017). Transient Opening of the Mitochondrial Permeability Transition Pore Induces Microdomain Calcium Transients in Astrocyte Processes. Neuron *93*, 587-605 e587.

Al-Mehdi, A.B., Pastukh, V.M., Swiger, B.M., Reed, D.J., Patel, M.R., Bardwell, G.C., Pastukh, V.V., Alexeyev, M.F., and Gillespie, M.N. (2012). Perinuclear mitochondrial clustering creates an oxidant-rich nuclear domain required for hypoxia-induced transcription. Sci Signal *5*, ra47.

Anand, R., Wai, T., Baker, M.J., Kladt, N., Schauss, A.C., Rugarli, E., and Langer, T. (2014). The i-AAA protease YME1L and OMA1 cleave OPA1 to balance mitochondrial fusion and fission. J Cell Biol *204*, 919-929.

Anderson, M.A., Burda, J.E., Ren, Y., Ao, Y., O'Shea, T.M., Kawaguchi, R., Coppola, G., Khakh, B.S., Deming, T.J., and Sofroniew, M.V. (2016). Astrocyte scar formation aids central nervous system axon regeneration. Nature *532*, 195-200.

Arruda, A.P., Pers, B.M., Parlakgul, G., Guney, E., Inouye, K., and Hotamisligil, G.S. (2014). Chronic enrichment of hepatic endoplasmic reticulum-mitochondria contact leads to mitochondrial dysfunction in obesity. Nat Med *20*, 1427-1435.

Bardehle, S., Kruger, M., Buggenthin, F., Schwausch, J., Ninkovic, J., Clevers, H., Snippert, H.J., Theis, F.J., Meyer-Luehmann, M., Bechmann, I.*, et al.* (2013). Live imaging of astrocyte responses to acute injury reveals selective juxtavascular proliferation. Nat Neurosci *16*, 580-586.

Baughman, J.M., Perocchi, F., Girgis, H.S., Plovanich, M., Belcher-Timme, C.A., Sancak, Y., Bao, X.R., Strittmatter, L., Goldberger, O., Bogorad, R.L.*, et al.* (2011). Integrative genomics identifies MCU as an essential component of the mitochondrial calcium uniporter. Nature *476*, 341-345.

Bazargani, N., and Attwell, D. (2016). Astrocyte calcium signaling: the third wave. Nat Neurosci *19*, 182-189.

Belanger, M., Allaman, I., and Magistretti, P.J. (2011). Brain energy metabolism: focus on astrocyte-neuron metabolic cooperation. Cell Metab *14*, 724-738.

Bindocci, E., Savtchouk, I., Liaudet, N., Becker, D., Carriero, G., and Volterra, A. (2017). Three-dimensional Ca2+ imaging advances understanding of astrocyte biology. Science *356*.

Boulay, A.C., Saubamea, B., Adam, N., Chasseigneaux, S., Mazare, N., Gilbert, A., Bahin, M., Bastianelli, L., Blugeon, C., Perrin, S.*, et al.* (2017). Translation in astrocyte distal processes sets molecular heterogeneity at the gliovascular interface. Cell discovery *3*, 17005.

Castejon, O.J. (2015). Biopathology of astrocytes in human traumatic and complicated brain injuries. Review and hypothesis. Folia neuropathologica *53*, 173-192.

Chen, H., Detmer, S.A., Ewald, A.J., Griffin, E.E., Fraser, S.E., and Chan, D.C. (2003). Mitofusins Mfn1 and Mfn2 coordinately regulate mitochondrial fusion and are essential for embryonic development. J Cell Biol *160*, 189-200.

Chen, H., McCaffery, J.M., and Chan, D.C. (2007). Mitochondrial fusion protects against neurodegeneration in the cerebellum. Cell *130*, 548-562.

Chen, K.H., Guo, X., Ma, D., Guo, Y., Li, Q., Yang, D., Li, P., Qiu, X., Wen, S., Xiao, R.P.*, et al.* (2004). Dysregulation of HSG triggers vascular proliferative disorders. Nat Cell Biol *6*, 872-883.

Chen, Q., Kirk, K., Shurubor, Y.I., Zhao, D., Arreguin, A.J., Shahi, I., Valsecchi, F., Primiano, G., Calder, E.L., Carelli, V.*, et al.* (2018). Rewiring of Glutamine Metabolism Is a Bioenergetic Adaptation of Human Cells with Mitochondrial DNA Mutations. Cell Metab *27*, 1007-1025 e1005.

Chow, L.M., Zhang, J., and Baker, S.J. (2008). Inducible Cre recombinase activity in mouse mature astrocytes and adult neural precursor cells. Transgenic research *17*, 919-928.

Cipolat, S., Martins de Brito, O., Dal Zilio, B., and Scorrano, L. (2004). OPA1 requires mitofusin 1 to promote mitochondrial fusion. Proc Natl Acad Sci U S A *101*, 15927-15932.

Csordas, G., Renken, C., Varnai, P., Walter, L., Weaver, D., Buttle, K.F., Balla, T., Mannella, C.A., and Hajnoczky, G. (2006). Structural and functional features and significance of the physical linkage between ER and mitochondria. J Cell Biol *174*, 915-921.

Csordas, G., Varnai, P., Golenar, T., Roy, S., Purkins, G., Schneider, T.G., Balla, T., and Hajnoczky, G. (2010). Imaging interorganelle contacts and local calcium dynamics at the ER-mitochondrial interface. Molecular cell *39*, 121-132.

Csordas, G., Weaver, D., and Hajnoczky, G. (2018). Endoplasmic Reticulum-Mitochondrial Contactology: Structure and Signaling Functions. Trends in cell biology *28*, 523-540.

de Brito, O.M., and Scorrano, L. (2008). Mitofusin 2 tethers endoplasmic reticulum to mitochondria. Nature *456*, 605-610.

De Stefani, D., Raffaello, A., Teardo, E., Szabo, I., and Rizzuto, R. (2011). A forty-kilodalton protein of the inner membrane is the mitochondrial calcium uniporter. Nature *476*, 336-340.

Dietrich, M.O., Liu, Z.W., and Horvath, T.L. (2013). Mitochondrial dynamics controlled by mitofusins regulate Agrp neuronal activity and diet-induced obesity. Cell *155*, 188-199.

Fiebig, C., Keiner, S., Ebert, B., Schaffner, I., Jagasia, R., Lie, D.C., and Beckervordersandforth, R. (2019). Mitochondrial Dysfunction in Astrocytes Impairs the Generation of Reactive Astrocytes and Enhances Neuronal Cell Death in the Cortex Upon Photothrombotic Lesion. Frontiers in molecular neuroscience *12*, 40.

Filadi, R., Greotti, E., Turacchio, G., Luini, A., Pozzan, T., and Pizzo, P. (2015). Mitofusin 2 ablation increases endoplasmic reticulum-mitochondria coupling. Proc Natl Acad Sci U S A *112*, E2174-2181.

Giorgi, C., Marchi, S., and Pinton, P. (2018). The machineries, regulation and cellular functions of mitochondrial calcium. Nat Rev Mol Cell Biol *19*, 713-730.

Gobel, J., Motori, E., and Bergami, M. (2018). Spatiotemporal control of mitochondrial network dynamics in astroglial cells. Biochemical and biophysical research communications *500*, 17-25.

Gomes, L.C., Di Benedetto, G., and Scorrano, L. (2011). During autophagy mitochondria elongate, are spared from degradation and sustain cell viability. Nat Cell Biol *13*, 589-598.

Gordon, G.R., Choi, H.B., Rungta, R.L., Ellis-Davies, G.C., and MacVicar, B.A. (2008). Brain metabolism dictates the polarity of astrocyte control over arterioles. Nature *456*, 745-749.

Guo, Y., Li, D., Zhang, S., Yang, Y., Liu, J.J., Wang, X., Liu, C., Milkie, D.E., Moore, R.P., Tulu, U.S.*, et al.* (2018). Visualizing Intracellular Organelle and Cytoskeletal Interactions at Nanoscale Resolution on Millisecond Timescales. Cell *175*, 1430-1442 e1417.

Hamby, M.E., Coppola, G., Ao, Y., Geschwind, D.H., Khakh, B.S., and Sofroniew, M.V. (2012). Inflammatory mediators alter the astrocyte transcriptome and calcium signaling elicited by multiple g-protein-coupled receptors. J Neurosci *32*, 14489-14510.

Han, S.M., Baig, H.S., and Hammarlund, M. (2016). Mitochondria Localize to Injured Axons to Support Regeneration. Neuron *92*, 1308-1323.

Hayashi, T., Rizzuto, R., Hajnoczky, G., and Su, T.P. (2009). MAM: more than just a housekeeper. Trends in cell biology *19*, 81-88.

Hertz, L., Peng, L., and Dienel, G.A. (2007). Energy metabolism in astrocytes: high rate of oxidative metabolism and spatiotemporal dependence on glycolysis/glycogenolysis. J Cereb Blood Flow Metab *27*, 219-249.

Herzig, S., and Shaw, R.J. (2018). AMPK: guardian of metabolism and mitochondrial homeostasis. Nat Rev Mol Cell Biol *19*, 121-135.

Iadecola, C. (2017). The Neurovascular Unit Coming of Age: A Journey through Neurovascular Coupling in Health and Disease. Neuron *96*, 17-42.

Ignatenko, O., Chilov, D., Paetau, I., de Miguel, E., Jackson, C.B., Capin, G., Paetau, A., Terzioglu, M., Euro, L., and Suomalainen, A. (2018). Loss of mtDNA activates astrocytes and leads to spongiotic encephalopathy. Nature communications *9*, 70.

Iliff, J.J., Wang, M., Liao, Y., Plogg, B.A., Peng, W., Gundersen, G.A., Benveniste, H., Vates, G.E., Deane, R., Goldman, S.A.*, et al.* (2012). A paravascular pathway facilitates CSF flow through the brain parenchyma and the clearance of interstitial solutes, including amyloid beta. Science translational medicine *4*, 147ra111.

Ishihara, N., Nomura, M., Jofuku, A., Kato, H., Suzuki, S.O., Masuda, K., Otera, H., Nakanishi, Y., Nonaka, I., Goto, Y.*, et al.* (2009). Mitochondrial fission factor Drp1 is essential for embryonic development and synapse formation in mice. Nat Cell Biol *11*, 958-966.

Jackson, J.G., and Robinson, M.B. (2015). Reciprocal Regulation of Mitochondrial Dynamics and Calcium Signaling in Astrocyte Processes. J Neurosci *35*, 15199-15213.

Khakh, B.S., and Sofroniew, M.V. (2015). Diversity of astrocyte functions and phenotypes in neural circuits. Nat Neurosci *18*, 942-952.

Kulkarni, S.S., Joffraud, M., Boutant, M., Ratajczak, J., Gao, A.W., Maclachlan, C., Hernandez-Alvarez, M.I., Raymond, F., Metairon, S., Descombes, P.*, et al.* (2016). Mfn1 Deficiency in the Liver Protects Against Diet-Induced Insulin Resistance and Enhances the Hypoglycemic Effect of Metformin. Diabetes *65*, 3552-3560.

Labbe, K., Murley, A., and Nunnari, J. (2014). Determinants and functions of mitochondrial behavior. Annual review of cell and developmental biology *30*, 357-391.

Lee, S., Sterky, F.H., Mourier, A., Terzioglu, M., Cullheim, S., Olson, L., and Larsson, N.G. (2012). Mitofusin 2 is necessary for striatal axonal projections of midbrain dopamine neurons. Human molecular genetics *21*, 4827-4835.

Li, H., Wang, X., Zhang, N., Gottipati, M.K., Parpura, V., and Ding, S. (2014). Imaging of mitochondrial Ca2+ dynamics in astrocytes using cell-specific mitochondria-targeted GCaMP5G/6s: mitochondrial Ca2+ uptake and cytosolic Ca2+ availability via the endoplasmic reticulum store. Cell calcium *56*, 457-466.

Liddelow, S.A., and Barres, B.A. (2017). Reactive Astrocytes: Production, Function, and Therapeutic Potential. Immunity *46*, 957-967.

Lopez-Fabuel, I., Le Douce, J., Logan, A., James, A.M., Bonvento, G., Murphy, M.P., Almeida, A., and Bolanos, J.P. (2016). Complex I assembly into supercomplexes determines differential mitochondrial ROS production in neurons and astrocytes. Proc Natl Acad Sci U S A *113*, 13063-13068.

Lovatt, D., Sonnewald, U., Waagepetersen, H.S., Schousboe, A., He, W., Lin, J.H., Han, X., Takano, T., Wang, S., Sim, F.J.*, et al.* (2007). The transcriptome and metabolic gene signature of protoplasmic astrocytes in the adult murine cortex. J Neurosci *27*, 12255-12266.

Luchsinger, L.L., de Almeida, M.J., Corrigan, D.J., Mumau, M., and Snoeck, H.W. (2016). Mitofusin 2 maintains haematopoietic stem cells with extensive lymphoid potential. Nature *529*, 528-531.

Mar, F.M., Simoes, A.R., Leite, S., Morgado, M.M., Santos, T.E., Rodrigo, I.S., Teixeira, C.A., Misgeld, T., and Sousa, M.M. (2014). CNS axons globally increase axonal transport after peripheral conditioning. J Neurosci *34*, 5965-5970.

Mathiisen, T.M., Lehre, K.P., Danbolt, N.C., and Ottersen, O.P. (2010). The perivascular astroglial sheath provides a complete covering of the brain microvessels: an electron microscopic 3D reconstruction. Glia *58*, 1094-1103.

Misgeld, T., Kerschensteiner, M., Bareyre, F.M., Burgess, R.W., and Lichtman, J.W. (2007). Imaging axonal transport of mitochondria in vivo. Nat Methods *4*, 559-561.

Mishra, A., Reynolds, J.P., Chen, Y., Gourine, A.V., Rusakov, D.A., and Attwell, D. (2016). Astrocytes mediate neurovascular signaling to capillary pericytes but not to arterioles. Nat Neurosci *19*, 1619-1627.

Moss, J., Gebara, E., Bushong, E.A., Sanchez-Pascual, I., O'Laoi, R., El M'Ghari, I., Kocher-Braissant, J., Ellisman, M.H., and Toni, N. (2016). Fine processes of Nestin-GFP-positive radial glia-like stem cells in the adult dentate gyrus ensheathe local synapses and vasculature. Proc Natl Acad Sci U S A *113*, E2536-2545.

Motori, E., Puyal, J., Toni, N., Ghanem, A., Angeloni, C., Malaguti, M., Cantelli-Forti, G., Berninger, B., Conzelmann, K.K., Gotz, M.*, et al.* (2013). Inflammation-induced alteration of astrocyte mitochondrial dynamics requires autophagy for mitochondrial network maintenance. Cell Metab *18*, 844-859.

Murley, A., and Nunnari, J. (2016). The Emerging Network of Mitochondria-Organelle Contacts. Molecular cell *61*, 648-653.

Naon, D., Zaninello, M., Giacomello, M., Varanita, T., Grespi, F., Lakshminaranayan, S., Serafini, A., Semenzato, M., Herkenne, S., Hernandez-Alvarez, M.I.*, et al.* (2016). Critical reappraisal confirms that Mitofusin 2 is an endoplasmic reticulum-mitochondria tether. Proc Natl Acad Sci U S A *113*, 11249-11254.

O'Donnell, J.C., Jackson, J.G., and Robinson, M.B. (2016). Transient Oxygen/Glucose Deprivation Causes a Delayed Loss of Mitochondria and Increases Spontaneous Calcium Signaling in Astrocytic Processes. J Neurosci *36*, 7109-7127.

Owens, K., Park, J.H., Gourley, S., Jones, H., and Kristian, T. (2015). Mitochondrial dynamics: cell-type and hippocampal region specific changes following global cerebral ischemia. Journal of bioenergetics and biomembranes *47*, 13-31.

Parnis, J., Montana, V., Delgado-Martinez, I., Matyash, V., Parpura, V., Kettenmann, H., Sekler, I., and Nolte, C. (2013). Mitochondrial exchanger NCLX plays a major role in the intracellular Ca2+ signaling, gliotransmission, and proliferation of astrocytes. J Neurosci *33*, 7206-7219.

Parpura, V., Grubisic, V., and Verkhratsky, A. (2011). Ca(2+) sources for the exocytotic release of glutamate from astrocytes. Biochim Biophys Acta *1813*, 984-991.

Petzold, G.C., Albeanu, D.F., Sato, T.F., and Murthy, V.N. (2008). Coupling of neural activity to blood flow in olfactory glomeruli is mediated by astrocytic pathways. Neuron *58*, 897-910.

Pfrieger, F.W., and Ungerer, N. (2011). Cholesterol metabolism in neurons and astrocytes. Progress in lipid research *50*, 357-371.

Polyzos, A.A., Lee, D.Y., Datta, R., Hauser, M., Budworth, H., Holt, A., Mihalik, S., Goldschmidt, P., Frankel, K., Trego, K.*, et al.* (2019). Metabolic Reprogramming in Astrocytes Distinguishes Region-Specific Neuronal Susceptibility in Huntington Mice. Cell Metab.

Rambold, A.S., Kostelecky, B., Elia, N., and Lippincott-Schwartz, J. (2011). Tubular network formation protects mitochondria from autophagosomal degradation during nutrient starvation. Proc Natl Acad Sci U S A *108*, 10190-10195.

Rangaraju, V., Lauterbach, M., and Schuman, E.M. (2019). Spatially Stable Mitochondrial Compartments Fuel Local Translation during Plasticity. Cell *176*, 73-84 e15.

Reyes, R.C., and Parpura, V. (2008). Mitochondria modulate Ca2+-dependent glutamate release from rat cortical astrocytes. J Neurosci *28*, 9682-9691.

Rizzuto, R., De Stefani, D., Raffaello, A., and Mammucari, C. (2012). Mitochondria as sensors and regulators of calcium signalling. Nat Rev Mol Cell Biol *13*, 566-578.

Schneeberger, M., Dietrich, M.O., Sebastian, D., Imbernon, M., Castano, C., Garcia, A., Esteban, Y., Gonzalez-Franquesa, A., Rodriguez, I.C., Bortolozzi, A.*, et al.* (2013). Mitofusin 2 in POMC neurons connects ER stress with leptin resistance and energy imbalance. Cell *155*, 172-187.

Schrepfer, E., and Scorrano, L. (2016). Mitofusins, from Mitochondria to Metabolism. Molecular cell *61*, 683-694.

Shigetomi, E., Bushong, E.A., Haustein, M.D., Tong, X., Jackson-Weaver, O., Kracun, S., Xu, J., Sofroniew, M.V., Ellisman, M.H., and Khakh, B.S. (2013). Imaging calcium microdomains within entire astrocyte territories and endfeet with GCaMPs expressed using adeno-associated viruses. The Journal of general physiology *141*, 633-647.

Shigetomi, E., Patel, S., and Khakh, B.S. (2016). Probing the Complexities of Astrocyte Calcium Signaling. Trends in cell biology *26*, 300-312.

Sprenger, H.G., Wani, G., Hesseling, A., Konig, T., Patron, M., MacVicar, T., Ahola, S., Wai, T., Barth, E., Rugarli, E.I.*, et al.* (2019). Loss of the mitochondrial i-AAA protease YME1L leads to ocular dysfunction and spinal axonopathy. EMBO molecular medicine *11*.

Stephen, T.L., Higgs, N.F., Sheehan, D.F., Al Awabdh, S., Lopez-Domenech, G., Arancibia-Carcamo, I.L., and Kittler, J.T. (2015). Miro1 Regulates Activity-Driven Positioning of Mitochondria within Astrocytic Processes Apposed to Synapses to Regulate Intracellular Calcium Signaling. J Neurosci *35*, 15996-16011.

Sterky, F.H., Lee, S., Wibom, R., Olson, L., and Larsson, N.G. (2011). Impaired mitochondrial transport and Parkin-independent degeneration of respiratory chain-deficient dopamine neurons in vivo. Proc Natl Acad Sci U S A *108*, 12937-12942.

Supplie, L.M., Duking, T., Campbell, G., Diaz, F., Moraes, C.T., Gotz, M., Hamprecht, B., Boretius, S., Mahad, D., and Nave, K.A. (2017). Respiration-Deficient Astrocytes Survive As Glycolytic Cells In Vivo. J Neurosci *37*, 4231-4242.

Sweeney, M.D., Ayyadurai, S., and Zlokovic, B.V. (2016). Pericytes of the neurovascular unit: key functions and signaling pathways. Nat Neurosci *19*, 771-783.

Takano, T., Tian, G.F., Peng, W., Lou, N., Libionka, W., Han, X., and Nedergaard, M. (2006). Astrocyte-mediated control of cerebral blood flow. Nat Neurosci *9*, 260-267.

Tran, C.H.T., Peringod, G., and Gordon, G.R. (2018). Astrocytes Integrate Behavioral State and Vascular Signals during Functional Hyperemia. Neuron *100*, 1133-1148 e1133.

Volterra, A., Liaudet, N., and Savtchouk, I. (2014). Astrocyte Ca(2)(+) signalling: an unexpected complexity. Nat Rev Neurosci *15*, 327-335.

Voskuhl, R.R., Peterson, R.S., Song, B., Ao, Y., Morales, L.B., Tiwari-Woodruff, S., and Sofroniew, M.V. (2009). Reactive astrocytes form scar-like perivascular barriers to leukocytes during adaptive immune inflammation of the CNS. J Neurosci *29*, 11511-11522.

Wang, X., Lou, N., Xu, Q., Tian, G.F., Peng, W.G., Han, X., Kang, J., Takano, T., and Nedergaard, M. (2006). Astrocytic Ca2+ signaling evoked by sensory stimulation in vivo. Nat Neurosci *9*, 816-823.

Wasilewski, M., Semenzato, M., Rafelski, S.M., Robbins, J., Bakardjiev, A.I., and Scorrano, L. (2012). Optic atrophy 1-dependent mitochondrial remodeling controls steroidogenesis in trophoblasts. Current biology : CB *22*, 1228-1234.

Wong, B.W., Marsch, E., Treps, L., Baes, M., and Carmeliet, P. (2017). Endothelial cell metabolism in health and disease: impact of hypoxia. EMBO J *36*, 2187-2203.

Wongkittichote, P., Ah Mew, N., and Chapman, K.A. (2017). Propionyl-CoA carboxylase - A review. Molecular genetics and metabolism *122*, 145-152.

Zamanian, J.L., Xu, L., Foo, L.C., Nouri, N., Zhou, L., Giffard, R.G., and Barres, B.A. (2012). Genomic analysis of reactive astrogliosis. J Neurosci *32*, 6391-6410.

Zariwala, H.A., Borghuis, B.G., Hoogland, T.M., Madisen, L., Tian, L., De Zeeuw, C.I., Zeng, H., Looger, L.L., Svoboda, K., and Chen, T.W. (2012). A Cre-dependent GCaMP3 reporter mouse for neuronal imaging in vivo. J Neurosci *32*, 3131-3141.

Zhao, Z., Nelson, A.R., Betsholtz, C., and Zlokovic, B.V. (2015). Establishment and Dysfunction of the Blood-Brain Barrier. Cell *163*, 1064-1078.

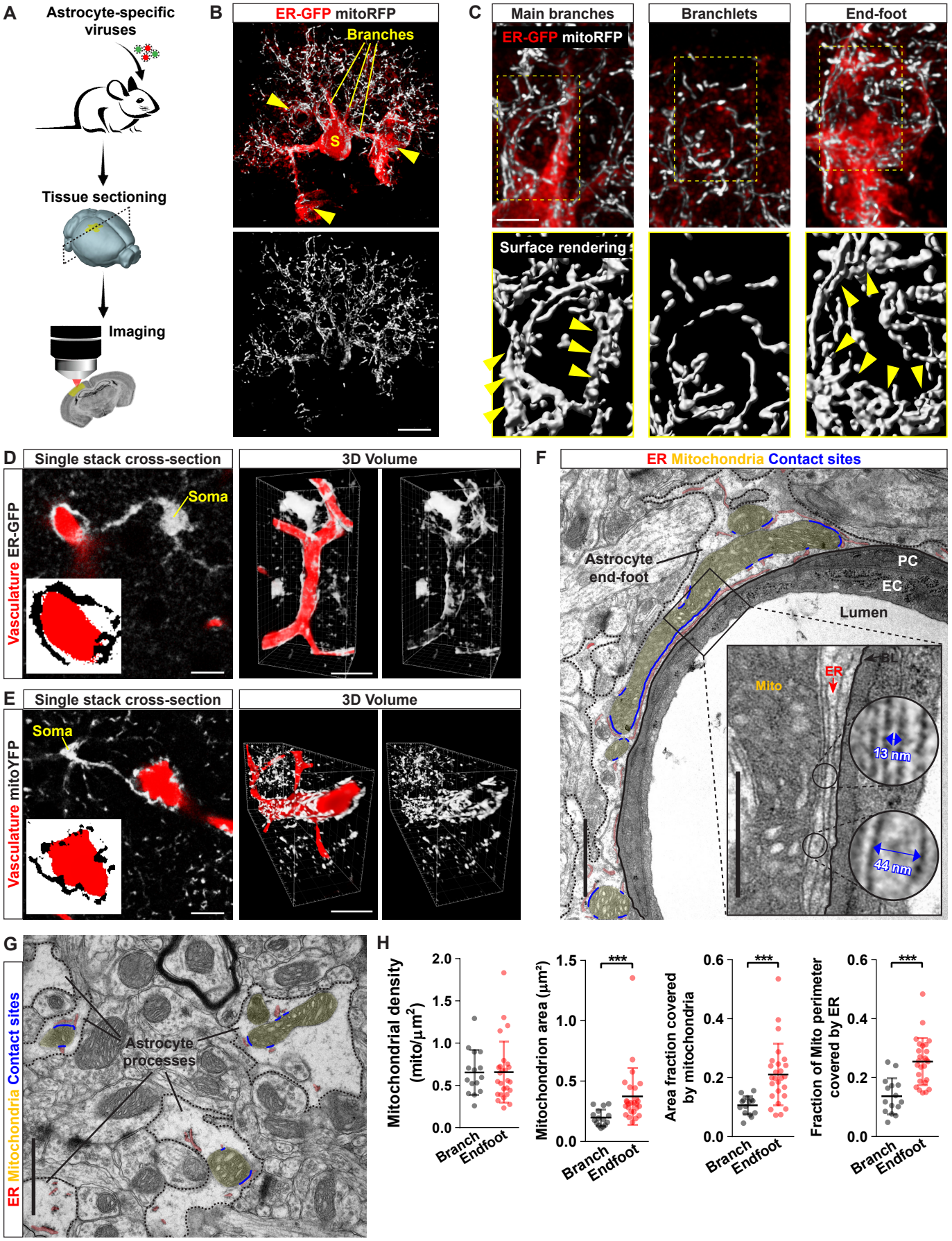
A
Astrocyte-specific viruses
Tissue sectioning
Imaging
B
ER-GFP mitoRFP
Branches
S
C
Main branches
Branchlets
End-foot
ER-GFP mitoRFP
Surface rendering
D
Single stack cross-section
3D Volume
Vasculature ER-GFP
Soma
E
Single stack cross-section
3D Volume
Vasculature mitoYFP
Soma
F
ER Mitochondria Contact sites
Astrocyte end-foot
PC
EC
Lumen
BL
Mito
ER
13 nm
44 nm
G
ER Mitochondria Contact sites
Astrocyte processes
H
Mitochondrial density (mito/µm²)
Mitochondrion area (µm²)
Area fraction covered by mitochondria
Fraction of Mito perimeter covered by ER
***
Branch
Endfoot

Figure 1

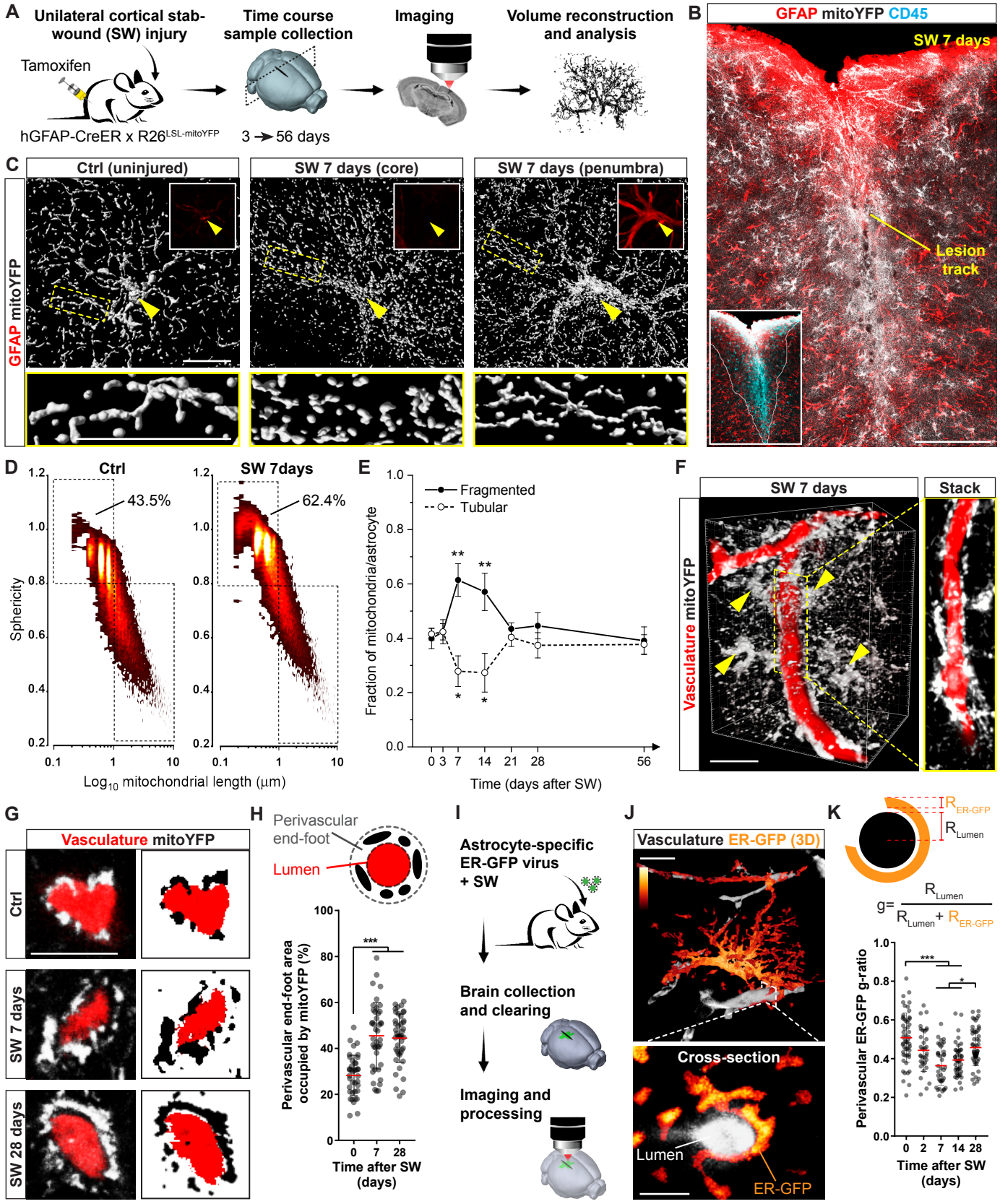
A
Unilateral cortical stab-wound (SW) injury
Tamoxifen
hGFAP-CreER x R26LSL-mitoYFP
Time course sample collection
3 → 56 days
Imaging
Volume reconstruction and analysis
B
GFAP mitoYFP CD45
SW 7 days
Lesion track
C
Ctrl (uninjured)
SW 7 days (core)
SW 7 days (penumbra)
GFAP mitoYFP
D
Ctrl
SW 7days
43.5%
62.4%
Sphericity
Log10 mitochondrial length (µm)
E
Fragmented
Tubular
Fraction of mitochondria/astrocyte
Time (days after SW)
F
SW 7 days
Stack
Vasculature mitoYFP
G
Vasculature mitoYFP
Ctrl
SW 7 days
SW 28 days
H
Perivascular end-foot
Lumen
Perivascular end-foot area occupied by mitoYFP (%)
Time after SW (days)
I
Astrocyte-specific ER-GFP virus + SW
Brain collection and clearing
Imaging and processing
J
Vasculature ER-GFP (3D)
Cross-section
Lumen
ER-GFP
K
RER-GFP
RLumen
g= RLumen / (RLumen + RER-GFP)
Perivascular ER-GFP g-ratio
Time after SW (days)

Figure 2

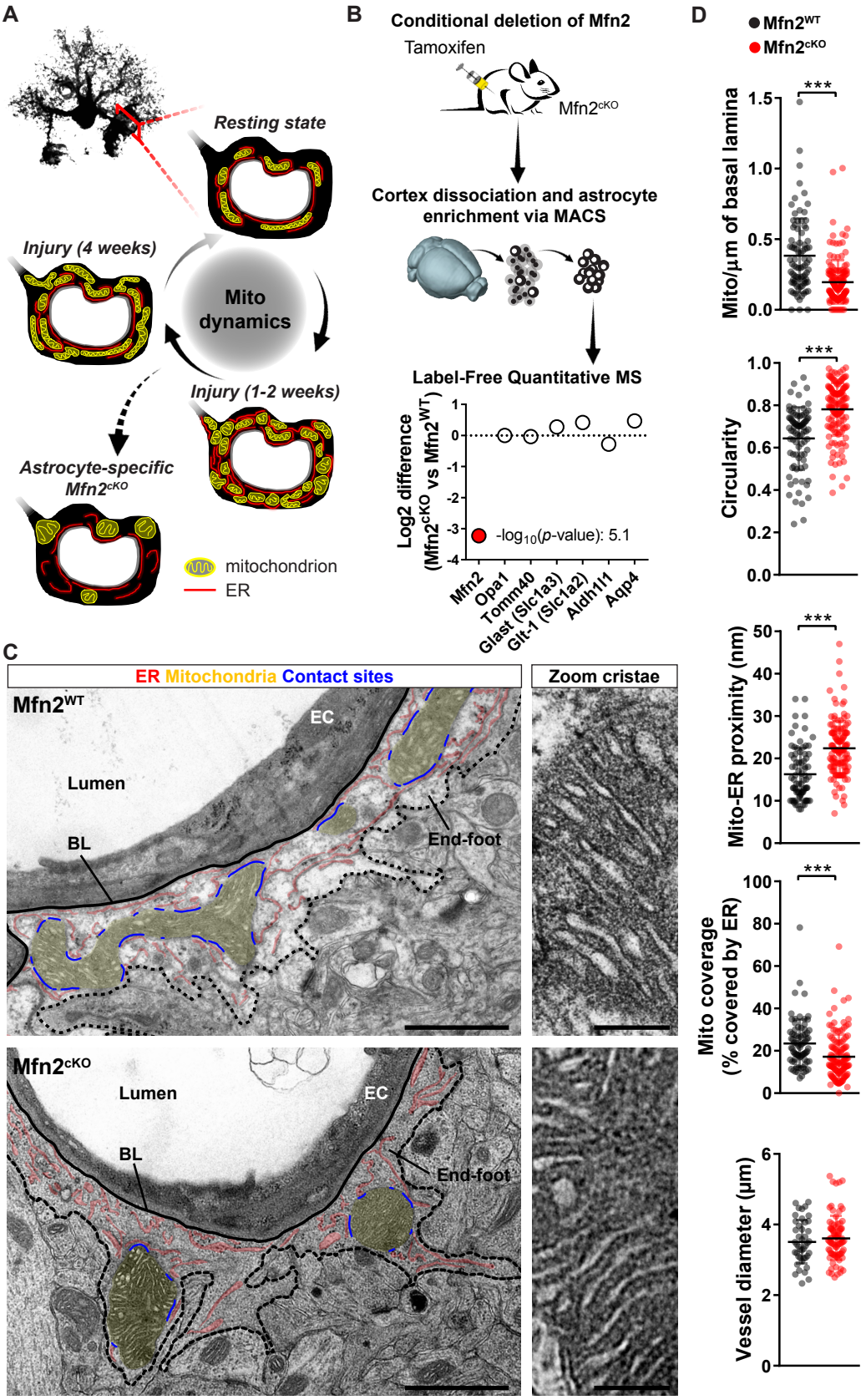
A
Resting state
Injury (4 weeks)
Mito dynamics
Injury (1-2 weeks)
Astrocyte-specific Mfn2cKO
mitochondrion
ER
B
Conditional deletion of Mfn2
Tamoxifen
Mfn2cKO
Cortex dissociation and astrocyte enrichment via MACS
Label-Free Quantitative MS
Log2 difference (Mfn2cKO vs Mfn2WT)
-log10(p-value): 5.1
Mfn2
Opa1
Tomm40
Glast (Slc1a3)
Glt-1 (Slc1a2)
Aldh1l1
Aqp4
C
ER Mitochondria Contact sites
Zoom cristae
Mfn2WT
EC
Lumen
BL
End-foot
Mfn2cKO
D
Mfn2WT
Mfn2cKO
Mito/µm of basal lamina
Circularity
Mito-ER proximity (nm)
Mito coverage (% covered by ER)
Vessel diameter (µm)
***

Figure 3

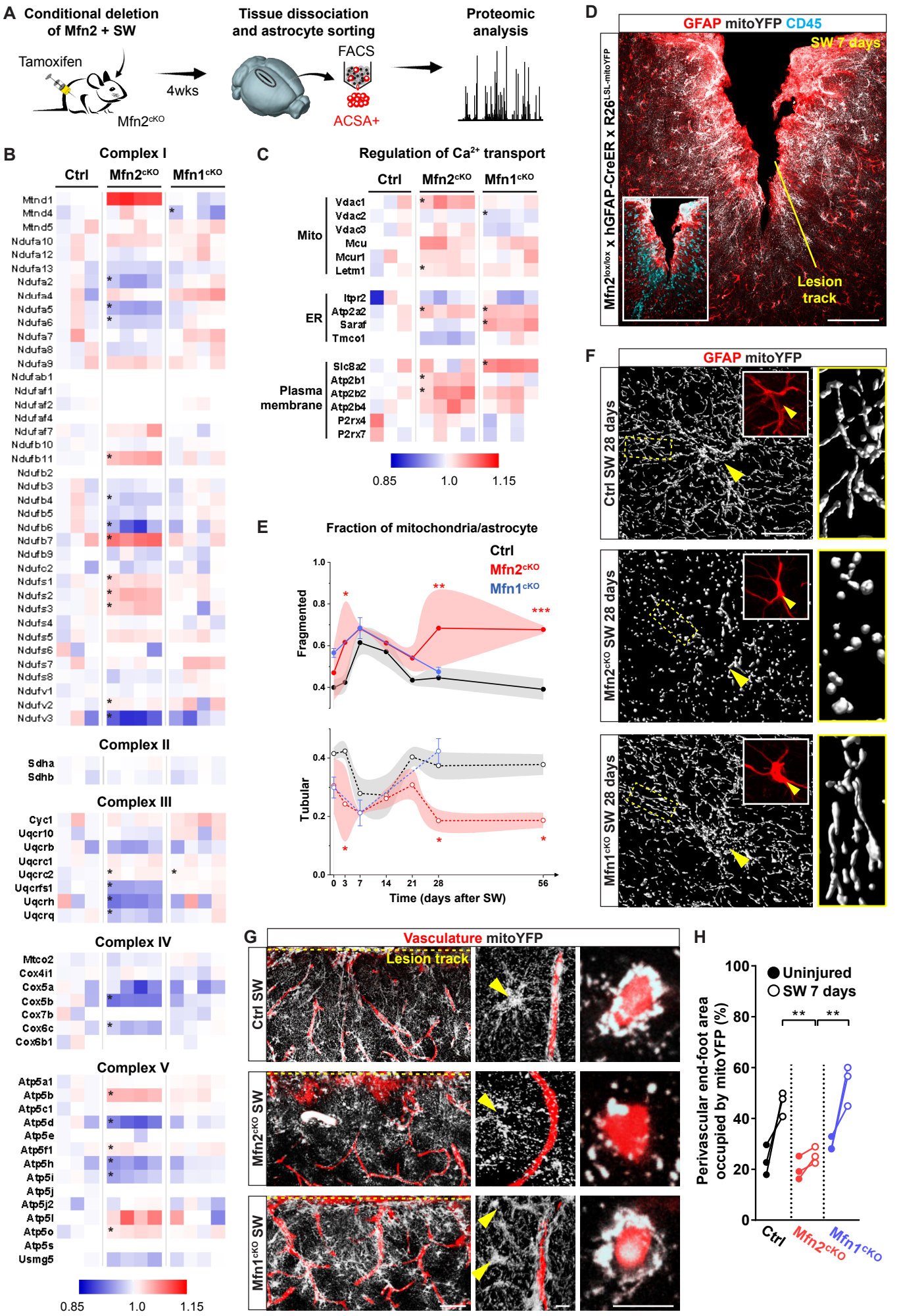
A
Conditional deletion of Mfn2 + SW
Tamoxifen
4wks
Mfn2cKO
Tissue dissociation and astrocyte sorting
FACS
ACSA+
Proteomic analysis
B
Complex I
Ctrl
Mfn2cKO
Mfn1cKO
Mtnd1
Mtnd4
Mtnd5
Ndufa10
Ndufa12
Ndufa13
Ndufa2
Ndufa4
Ndufa5
Ndufa6
Ndufa7
Ndufa8
Ndufa9
Ndufab1
Ndufaf1
Ndufaf2
Ndufaf4
Ndufaf7
Ndufb10
Ndufb11
Ndufb2
Ndufb3
Ndufb4
Ndufb5
Ndufb6
Ndufb7
Ndufb9
Ndufc2
Ndufs1
Ndufs2
Ndufs3
Ndufs4
Ndufs5
Ndufs6
Ndufs7
Ndufs8
Ndufv1
Ndufv2
Ndufv3
Complex II
Sdha
Sdhb
Complex III
Cyc1
Uqcr10
Uqcrb
Uqcrc1
Uqcrc2
Uqcrfs1
Uqcrh
Uqcrq
Complex IV
Mtco2
Cox4i1
Cox5a
Cox5b
Cox7b
Cox6c
Cox6b1
Complex V
Atp5a1
Atp5b
Atp5c1
Atp5d
Atp5e
Atp5f1
Atp5h
Atp5i
Atp5j
Atp5j2
Atp5l
Atp5o
Atp5s
Usmg5
0.85
1.0
1.15
C
Regulation of Ca2+ transport
Ctrl
Mfn2cKO
Mfn1cKO
Mito
Vdac1
Vdac2
Vdac3
Mcu
Mcur1
Letm1
ER
Itpr2
Atp2a2
Saraf
Tmco1
Plasma membrane
Slc8a2
Atp2b1
Atp2b2
Atp2b4
P2rx4
P2rx7
0.85
1.0
1.15
E
Fraction of mitochondria/astrocyte
Ctrl
Mfn2cKO
Mfn1cKO
Fragmented
Tubular
Time (days after SW)
D
GFAP mitoYFP CD45
SW 7 days
Mfn2lox/lox x hGFAP-CreER x R26LSL-mitoYFP
Lesion track
F
GFAP mitoYFP
Ctrl SW 28 days
Mfn2cKO SW 28 days
Mfn1cKO SW 28 days
G
Vasculature mitoYFP
Lesion track
Ctrl SW
Mfn2cKO SW
Mfn1cKO SW
H
Uninjured
SW 7 days
Perivascular end-foot area occupied by mitoYFP (%)
Ctrl
Mfn2cKO
Mfn1cKO

Figure 4

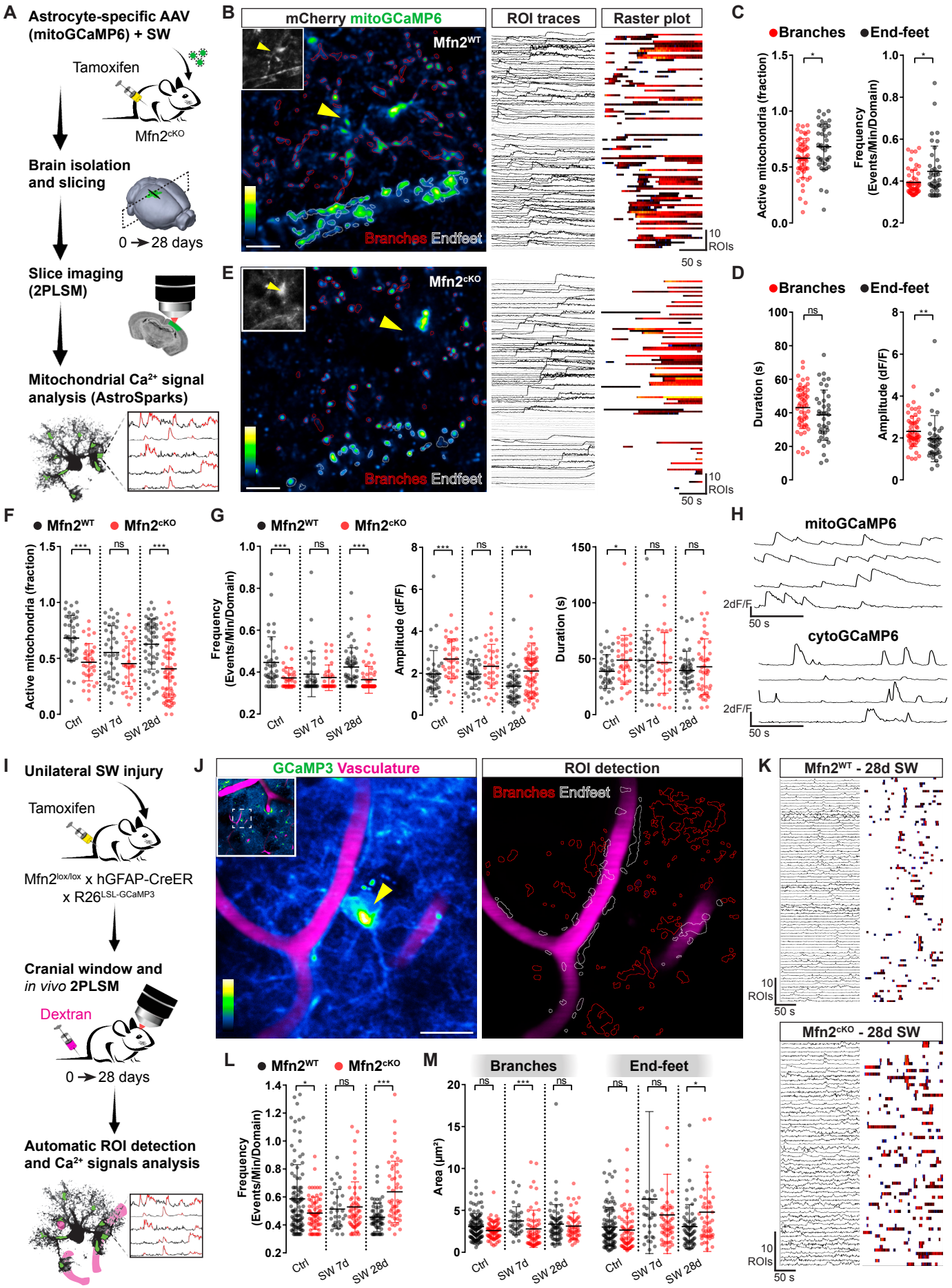
A
Astrocyte-specific AAV (mitoGCaMP6) + SW
Tamoxifen
Mfn2cKO
Brain isolation and slicing
0 → 28 days
Slice imaging (2PLSM)
Mitochondrial Ca2+ signal analysis (AstroSparks)
B
mCherry mitoGCaMP6
ROI traces
Raster plot
Mfn2WT
Branches Endfeet
10 ROIs
50 s
C
Branches End-feet
Active mitochondria (fraction)
Frequency (Events/Min/Domain)
D
Duration (s)
Amplitude (dF/F)
E
Mfn2cKO
F
Mfn2WT Mfn2cKO
Ctrl SW 7d SW 28d
G
H
mitoGCaMP6
cytoGCaMP6
2dF/F
50 s
I
Unilateral SW injury
Tamoxifen
Mfn2lox/lox x hGFAP-CreER x R26LSL-GCaMP3
Cranial window and in vivo 2PLSM
Dextran
0 → 28 days
Automatic ROI detection and Ca2+ signals analysis
J
GCaMP3 Vasculature
ROI detection
K
Mfn2WT - 28d SW
Mfn2cKO - 28d SW
L
M
Branches
End-feet
Area (µm²)

Figure 5

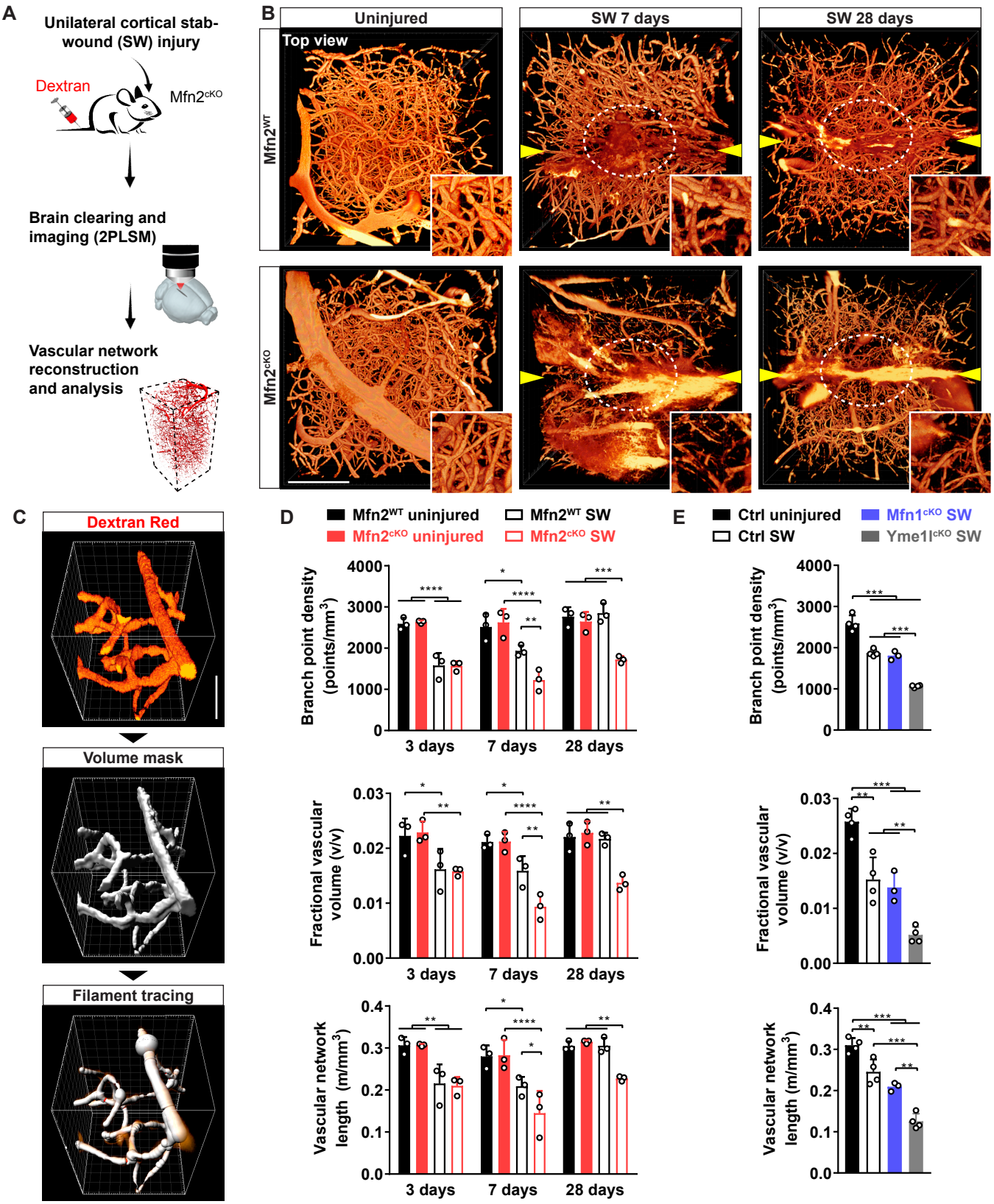
A
Unilateral cortical stab-wound (SW) injury
Dextran
Mfn2cKO
Brain clearing and imaging (2PLSM)
Vascular network reconstruction and analysis
B
Uninjured
SW 7 days
SW 28 days
Top view
Mfn2WT
Mfn2cKO
C
Dextran Red
Volume mask
Filament tracing
D
Mfn2WT uninjured
Mfn2cKO uninjured
Mfn2WT SW
Mfn2cKO SW
Branch point density (points/mm3)
Fractional vascular volume (v/v)
Vascular network length (m/mm3)
3 days
7 days
28 days
E
Ctrl uninjured
Ctrl SW
Mfn1cKO SW
Yme1lcKO SW

Figure 6

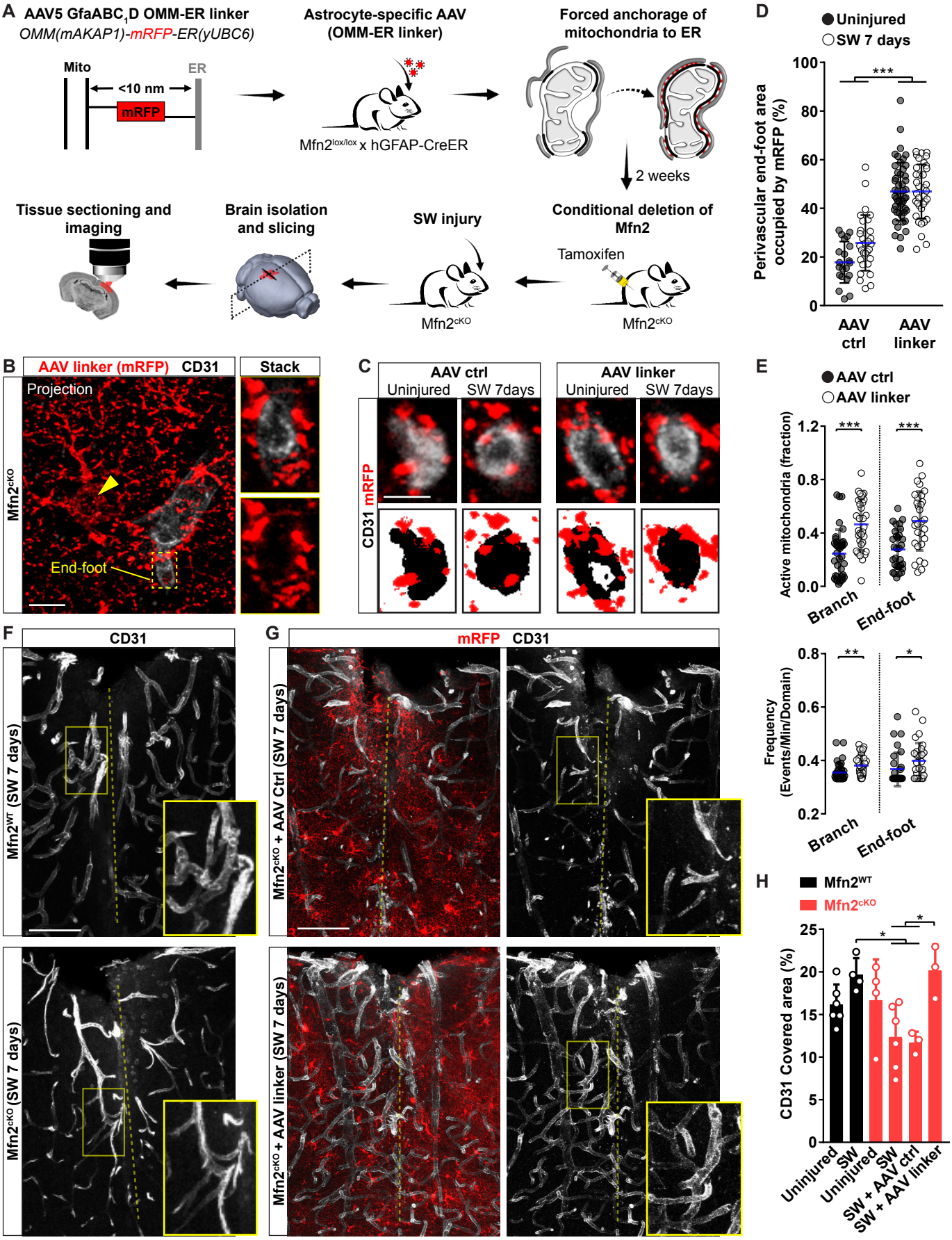
A
AAV5 GfaABC1D OMM-ER linker
OMM(mAKAP1)-mRFP-ER(yUBC6)
Mito
ER
<10 nm
mRFP
Astrocyte-specific AAV (OMM-ER linker)
Mfn2lox/lox x hGFAP-CreER
Forced anchorage of mitochondria to ER
2 weeks
Conditional deletion of Mfn2
Tamoxifen
Mfn2cKO
SW injury
Brain isolation and slicing
Tissue sectioning and imaging
B
AAV linker (mRFP)
CD31
Stack
Projection
Mfn2cKO
End-foot
C
AAV ctrl
AAV linker
Uninjured
SW 7days
CD31 mRFP
D
Uninjured
SW 7 days
Perivascular end-foot area occupied by mRFP (%)
AAV ctrl
AAV linker
E
AAV ctrl
AAV linker
Active mitochondria (fraction)
Branch
End-foot
Frequency (Events/Min/Domain)
F
CD31
Mfn2WT (SW 7 days)
Mfn2cKO (SW 7 days)
G
mRFP
CD31
Mfn2cKO + AAV Ctrl (SW 7 days)
Mfn2cKO + AAV linker (SW 7 days)
H
Mfn2WT
Mfn2cKO
CD31 Covered area (%)
Uninjured
SW
Uninjured
SW
SW + AAV ctrl
SW + AAV linker

Figure 7